

ESD RECORD COPY

RETURN TO
SCIENTIFIC & TECHNICAL INFORMATION DIVISION
(ESTI), BUILDING 1211

ESD ACCESSION LIST

ESTI Call No. AL 53388Copy No. 1 of 2 cys.ESD-TR-66-403
ESTI FILE COPY

3

Solid State Research**1966**

Prepared under Electronic Systems Division Contract AF 19(628)-5167 by

Lincoln Laboratory

MASSACHUSETTS INSTITUTE OF TECHNOLOGY

Lexington, Massachusetts

**BEST
SCAN
AVAILABLE**
ADOL041498

The work reported in this document was performed at Lincoln Laboratory,
a center for research operated by Massachusetts Institute of Technology,
with the support of the U.S. Air Force under Contract AF 19(628)-5167.

This report may be reproduced to satisfy needs of U.S. Government agencies.

Distribution of this document is unlimited.

Non-Lincoln Recipients
PLEASE DO NOT RETURN

Permission is given to destroy this document
when it is no longer needed.

3

1966

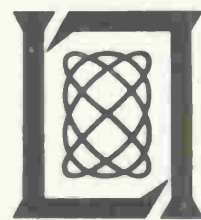
Solid State Research

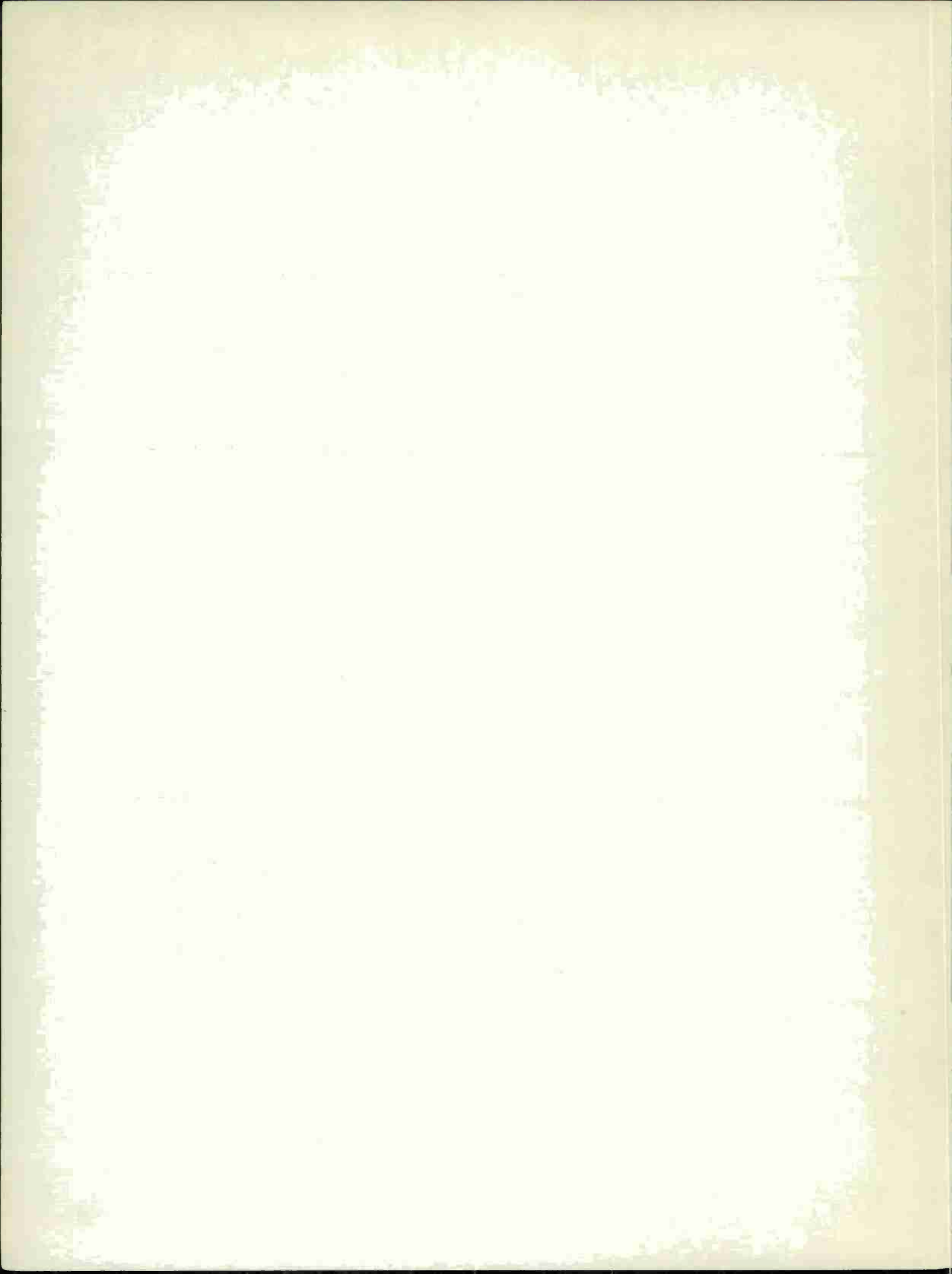
Issued 11 October 1966

Lincoln Laboratory

MASSACHUSETTS INSTITUTE OF TECHNOLOGY

Lexington, Massachusetts

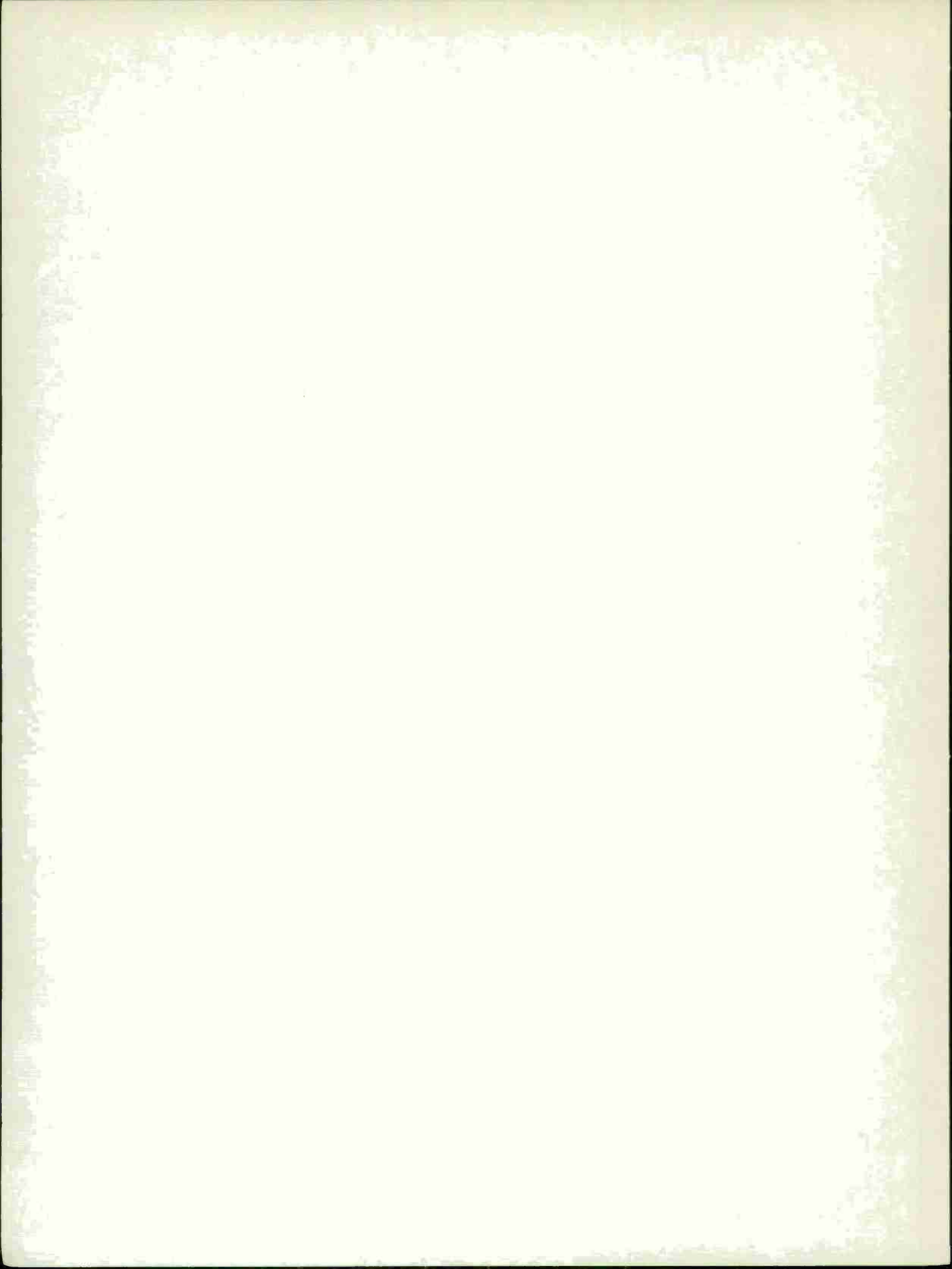




ABSTRACT

This report covers in detail the solid state research work at Lincoln Laboratory for the period 1 May through 31 July 1966. The topics covered are Solid State Device Research, Optical Techniques and Devices, Materials Research, and Physics of Solids.

Accepted for the Air Force
Franklin C. Hudson
Chief, Lincoln Laboratory Office



INTRODUCTION

I. SOLID STATE DEVICE RESEARCH

Laser emission has been observed in the wavelength region between 11 and 16μ in several $\text{Pb}_x\text{Sn}_{1-x}\text{Te}$ alloys at 12°K , optically excited by radiation from a GaAs diode laser. Coherent emission was obtained from a $\text{Pb}_{0.86}\text{Sn}_{0.14}\text{Te}$ alloy sample at 11.6μ , from a $\text{Pb}_{0.83}\text{Sn}_{0.17}\text{Te}$ sample at 14.9μ and from a $\text{Pb}_{0.81}\text{Sn}_{0.19}\text{Te}$ sample at 15.9μ . A model of the band structure of the $\text{Pb}_x\text{Sn}_{1-x}\text{Te}$ alloy system has been proposed to explain the composition dependence of the band gap and the change in sign of the temperature coefficient of the band gap between PbTe and SnTe. According to our proposed band model, with increasing Sn composition the energy gap of $\text{Pb}_x\text{Sn}_{1-x}\text{Te}$ initially decreases, goes to zero at some intermediate composition where the valence and conduction band edges become degenerate, and then increases, with the previous valence band now forming the conduction band edge and previous conduction band forming the valence band edge.

Laser emission has also been observed in the ultraviolet at several wavelengths between 3245 and 3300\AA at both liquid helium and nitrogen temperatures from ZnS single crystals pumped by an electron beam. Peak output power of 1.7 W has been obtained with a power efficiency of 6.5 percent. As many as 10 different laser lines have been observed to emanate from a single sample at irregularly spaced wavelength intervals in this region. It was determined that these laser lines were emitted from different points on the cavity face. Each line presumably corresponds to a different laser filament, and the spatial variation in wavelength is most probably caused by crystal inhomogeneities. With high spectral resolution each of the different laser lines exhibits the familiar Fabry-Perot cavity mode structure. Because of the very large dispersion of the refractive index of ZnS near the energy gap, the mode spacing decreases rapidly with decreasing wavelength, from a value of 0.3\AA at 3291\AA to 0.16\AA at 3245\AA .

By using an electron beam, we have also obtained laser emission from ZnO with a peak output power of 1 W and an efficiency of 1.3 percent at 4.2°K , and a peak output power of 0.5 W with an efficiency of 0.5 percent at 77°K .

CdS electron-beam-pumped lasers have had consistently higher threshold currents and lower power efficiencies than CdSe and $\text{CdS}_x\text{Se}_{1-x}$, with x as large as 0.9. Using some new CdS platelets, we have now obtained CdS electron-beam-pumped lasers with thresholds and efficiencies more nearly in line with those of the other II-VI semiconductor lasers.

Xenon flashlamp pumping of semiconductor lasers was extended to shorter wavelengths and higher temperatures. Laser emission has been observed from InSb at liquid helium temperature and from CdSe, $\text{CdS}_{0.6}\text{Se}_{0.4}$, and CdS at both liquid helium and liquid nitrogen temperatures. The thresholds are comparable with those obtained in electron beam pumping and in InSb with diodes of this material.

Introduction

The emission spectra at several injection levels have been obtained from diode lasers of PbS, PbTe, and PbSe. The emission spectra for the three materials are similar and remain unchanged with increasing injection level. The invariance of spectral shapes and peak positions with increasing diode current suggests an absence of band filling and that injected carriers may be nondegenerate, even at laser threshold.

II. OPTICAL TECHNIQUES AND DEVICES

The electro-optic effect has been observed in crystalline selenium (32 point-group symmetry) for 10.6- μm radiation; the value of the coefficient r_{11} was measured to be $\sim 2.5 \times 10^{-10} \text{ cm/V}$. Trigonal selenium, which is uniaxial and piezoelectric, appears to be the first elemental crystal in which the electro-optic effect has been observed. The value given above is in agreement with a phenomenological theory of optical harmonic generation, optical rectification, and the linear electro-optic effect set forth by R. C. Miller in 1964.

A high-power pulsed ruby laser has been used to range on retroreflector-equipped satellites at ranges up to 1000 nm. The laser and associated receiver were pointed at the targets, using a slave-tracking interconnection with the Millstone radar.

III. MATERIALS RESEARCH

Metal solution calorimetry has been used to determine the heat of formation for InSb(III), the new high-pressure phase reported recently, as well as the heats of formation for atmospheric pressure InSb(I) and high pressure InSb(II). The results of x-ray diffraction and superconducting transition temperature measurements show that InSb(III) is not the same as the orthorhombic high-pressure phase of InSb.

The resistivity of MnAs at 77°K has been measured as a function of hydrostatic pressure. The data show that at this temperature the B8 structure stable at atmospheric pressure is transformed into the B31 structure at 4.5 kbars. This result confirms the conclusion that above 4.5 kbars the B31 structure is stable down to the lowest temperatures.

Negative magnetoresistance has been observed at 4.2° and 77°K in single crystals of Ti_2O_3 doped with 1 to 3 atomic percent V. At 4.2°K, the resistivity is reduced by about 10 percent at 170 kG, the highest magnetic field employed. The negative magnetoresistance is attributed to the presence of V with localized magnetic moments.

On the basis of x-ray diffraction and electrical conductivity data for LaCoO_3 , the first-order phase change which occurs in this compound at 937°C has been identified as a localized-electron \rightarrow collective-electron transition. The x-ray results show that the crystal space group is $R\bar{3}c$ below 375°C and $R\bar{3}$ above this temperature. Ordering of high-spin and low-spin Co ions occurs on the two types of octahedral Co sites distinguishable in the $R\bar{3}$ symmetry.

X-ray diffraction studies have shown that PbRuO_3 has a modified pyrochlore structure containing ordered oxygen vacancies, which act as electron traps. The structure is

stabilized by trap-mediated cation-cation bonds between the four lead ions neighboring each oxygen vacancy.

Laser action has been observed in $\text{YVO}_4:\text{Nd}$ rods at pulsed thresholds of 2-3J, which are comparable to those obtained for YAG:Nd lasers. The strong yellow fluorescence excited by 2537 or 3660 \AA radiation in pure YVO_4 is completely quenched in $\text{YVO}_4:\text{Nd}$ crystals. The quenching is attributed to energy transfer from the host lattice to the Nd^{+3} ions.

An analytical method based on automatic potentiometric EDTA titrations has been developed for the determination of Pb and Sn in PbTe-SnTe alloys. Accuracies of 1 to 2 parts per 1000 have been obtained for titrant volumes in the 2- to 10-ml range.

IV. PHYSICS OF SOLIDS

Sensitive modulation techniques are being used to study the reflectivity and the magneto-reflectivity of solids in the vacuum ultraviolet, visible, and near-infrared regions of the spectrum. In addition to the magneto-piezo-optical technique which was reported in the last Solid State Research Report, studies have been initiated using electroreflectance, by means of an electrolyte, magneto-electroreflectance, and also modulation by passing pulsed electric currents through a sample. Our experimental results suggest that the latter effect is due to thermal modulation. Preliminary room temperature results in germanium, InSb, and GaSb have demonstrated an impressive enhancement of the resonances associated with interband transitions across energy gaps. Furthermore, it has been demonstrated that the electroreflectance technique works as well in metals as it does in semiconductors.

Far-infrared studies of the Zeeman effect in germanium doped with the Group III impurity gallium have now been extended to high magnetic fields. Additional splittings of the lines have been observed.

The study of propagation of 9-GHz longitudinal ultrasonic waves in n-InSb at low temperatures and magnetic fields up to 25 kG has been completed. This experiment has yielded a direct determination of the magnitude of the piezoelectric constant e_{14} and the conduction-band deformation potential C_1 .

Recently observed nonlinearities in the interband magneto-absorption in InSb have been interpreted in terms of electron-LO phonon interaction on the conduction-band Landau levels. However, the high-field magneto-absorption states may be almost entirely bound exciton-like; the effect of electron-phonon interaction on the energy of the bound exciton states in strong magnetic fields is now being investigated.

Using the Slater-Koster technique, secular determinants have been set up for TiO_2 , TiO , TiN and TiC. Transfer integrals have been evaluated for the last three materials.

Previous investigators have usually reported a local maximum in the susceptibility of LaCoO_3 at 90°K, except for one recent single crystal study. Our study indicates that the magnetic properties of this chemically pure material are strongly dependent on the

Introduction

method of preparation. Samples have been obtained which exhibit the susceptibility maximum, and this maximum can be removed by additional regrinding and refiring.

X-band magnetic resonance linewidth studies of polycrystalline ferromagnetic chalcogenides are continuing. The temperature dependence of the resonance linewidth has been measured for CdCr_2Se_4 and CdCr_2S_4 .

Antiferromagnetic resonance has been observed at millimeter wavelengths in the normal cubic spinels ZnCr_2Se_4 and ZnCr_2S_4 . In ZnCr_2Se_4 , a discontinuity was observed in the resonance field at the Néel temperature suggesting a first-order transition. No such discontinuity was found in ZnCr_2S_4 , and the temperature dependence of the resonance suggests a second-order transition.

Calculations by means of high temperature expansion techniques of properties of a classical Heisenberg magnet are continuing. Contrary to proposals by others, it is found that the form of the divergence of the zero-field static susceptibility does depend on the spin quantum number S. Furthermore, evidence is presented that a phase transition exists just as convincingly in the two-dimensional Heisenberg model with nearest-neighbor ferromagnetic interactions as in the three-dimensional case.

A proof has been given of the virial theorem for a homogeneous interacting electron gas in a uniform background of positive charge.

A perturbation-type calculation shows that for a large class of orbitals the ground Slater determinant of minimum energy for the H^- ion is not a bound state.

Theoretical analysis of the possible improvement in the efficiency of energy conversion by using inhomogeneously alloyed materials is under way.

Stimulated Brillouin scattering in single crystal quartz has been studied in the temperature range 2.1 to 300°K. Contrary to recently reported Russian work, no increase in the Stokes shift is found at temperatures below 80°K.

The study of the temperature dependence of second-harmonic incoherent scattering is continuing. A calculation which includes internal optical and static fields but neglects orientation correlation explains qualitatively, via the fourth-rank susceptibility tensor, the rapid decrease of scattering observed in CCl_4 on approach to boiling.

Raman scattering from charge carrier plasmons has been observed for the first time in a solid. The results have verified the recently predicted theoretical behavior of a plasmon-phonon system.

First-order infrared Raman spectra have been observed for the first time in solids: the materials studied have been GaAs, InP, AlSb and GaP. Up to now, Raman scattering had not been observed in the first three of these semiconductors.

The Raman cross section for light scattering by electrons making transitions between Landau levels in the conduction band of a semiconductor has been calculated, and appears for InSb to be two orders of magnitude greater than previously published estimates which neglected the effects of degenerate valence bands.

CONTENTS

Abstract	iii
Introduction	v
Organization	xi
Reports by Authors Engaged in Solid State Research	xii
I. SOLID STATE DEVICE RESEARCH	1
A. Band Structure and Laser Action in $Pb_xSn_{1-x}Te$	1
B. Efficient Ultraviolet Laser Emission in Electron Beam Excited ZnS	4
C. Electron Beam Pumped Lasers of ZnO and CdS	7
D. Flashlamp Pumping of Semiconductor Lasers	9
E. Emission Spectra of Pb Salt Diode Lasers	9
II. OPTICAL TECHNIQUES AND DEVICES	13
A. Electro-Optic Effect in Trigonal Selenium at $10.6\mu m$	13
B. Ruby Laser Radar	13
III. MATERIALS RESEARCH	15
A. High-Pressure Phases of InSb	15
B. Pressure Dependence of $B8 \rightleftharpoons B31$ Transition Temperature in MnAs	17
C. Negative Magnetoresistance in Ti_2O_3	18
D. First-Order Localized-Electron \rightleftharpoons Collective-Electron Transition in $LaCoO_3$	19
E. Trap-Mediated Cation-Cation Bond in $PbRuO_3$ Structure	20
F. $YVO_4:Nd$ Laser	22
G. Wet Chemical Analysis of PbTe-SnTe Alloys	23
IV. PHYSICS OF SOLIDS	25
A. Electronic Band Structure	25
1. Electroreflectance in Metallic Oxides	25
2. Modulated Reflectance of Germanium in the Ultraviolet	26
3. Electroreflectance in Metals	27
4. Infrared Magneto-Electroreflectance in Germanium, $GaSb$, and $InSb$	27
5. Magneto-Piezo-Optical Studies in Semiconductors	27
6. Far Infrared Zeeman Effect of Group III Impurities in Germanium	31
7. Electron-Phonon Interaction in $n-InSb$ at 9 GHz	32
8. Effect of Electron-Longitudinal Optical Phonon Interaction on Energy of Bound Exciton States in a Magnetic Field	35
9. Band Structure of TiO_2 in the LCAO Approximation	36
10. Band Structure Calculations on TiO , TiN , and TiC	36

Contents

B. Magnetism	37
1. Low-Temperature Crystallographic and Magnetic Study of LaCoO ₃	37
2. Microwave Resonance in Ferromagnetic Chalcogenides	39
3. Magnetic Resonance in Spiral Spinels	39
4. High Temperature Expansion of the Spin Correlation Function for the Classical Heisenberg Model	39
5. Dependence of the Critical Properties of Heisenberg Magnets on Spin and Lattice	41
6. Possibility of a Phase Transition for the Two-Dimensional Heisenberg Ferromagnet	41
C. Transport Theory	42
1. Virial Theorem for the Homogeneous Electron Gas	42
2. Minimum Energy Slater Determinant for H ⁻	42
3. Energy Conversion in Nonhomogeneous Materials	43
D. Scattering Experiments with Lasers	44
1. Stimulated Brillouin Scattering in Quartz at 2.1° to 300 °K	44
2. Second Harmonic Rayleigh Scattering in Liquids	45
3. Raman Scattering from Plasmons Interacting with LO Phonons in GaAs	48
4. First-Order Raman Effect in III-V Compounds	51
5. Landau Level Raman Scattering	52

ORGANIZATION

SOLID STATE DIVISION

A. L. McWhorter, Head
P. E. Tannenwald, Associate Head
M. J. Hudson, Assistant
E. P. Warekois
*D. T. Stevenson**

SOLID STATE THEORY

H. J. Zeiger, Leader
M. M. Litvak, Assistant Leader

Argyres, P. N.	Mason, V. J.
Chinn, S. R. [†]	Mason, W. C.
Dresselhaus, G. F.	Melanson, G. S., Jr.
Fleming, P. D. [†]	Palm, B. J.*
Kaplan, T. A.	Stanley, H. E.*
Kelley, P. L.	Trent, P. H.
Kleiner, W. H.	Van Zandt, L. L.
Larsen, D. M.	

OPTICS AND INFRARED

R. H. Kingston, Leader
R. J. Keyes, Assistant Leader

Bates, D. H.	Longaker, P. R.
Bostick, H. A.	McGowan, J.
Carbone, R. J.	McPhie, J. M.
Dennis, J. H.	Teich, M.C.
Freed, C.	Zimmerman, M. D.
Kaplan, T. [†]	

ELECTRONIC MATERIALS

J. B. Goodenough, Leader
J. M. Honig, Associate Leader
A. J. Strauss, Assistant Leader

Anderson, G. H., Jr.	Germann, R. W.
Andrews, H. I. [‡]	Hilsenrath, S.
Arnott, R. J.	Iseler, G. W.
Banus, M. D.	Kafalas, J. A.
Batson, D.	LaFleur, W. J.
Brebrick, R. F., Jr.	Lavine, M. C.*
Button, M. J.	Longo, J. M.
Cornwell, J. C.	O'Connor, J. R.
Delaney, E. J.	Owens, E. B.
Ehlers, H. H.	Plonko, M. C.
Esterling, D. M. [†]	Pollard, E. R. [‡]
Fahey, R. E.	Raccah, P. M.
Farrell, L. B.	Reed, T. B. [§]
Ferretti, A.	Roddy, J. T.
Finn, M. C.	Sohn, J. B.
Galvani, M. A.	

SOLID STATE PHYSICS

J. G. Mavroides, Leader
G. B. Wright, Assistant Leader

Bermon, S.	Krag, W. E.
Burke, J. W.	Mastromattei, E. L.
Buss, D. D. [†]	Menyuk, N.
Carman, R. L.*	Murphy, H. C.
Cohen, E. J. [†]	Nill, K. W.
Dickey, D. H.	Parker, C. D.
Dresselhaus, M. S.	Perry, F. H.
Dwight, K., Jr.	Scouler, W. J.
Feinleib, J.	Stickler, J. J. [‡]
Feldman, B.	Strahm, N. D. [‡]
Fulton, M. J.	Thaxter, J. B.
Groves, S. H.	Weber, R.
Johnson, E. J.	Weinberg, D. L.
Kernan, W. C.	Wyatt, P. W. [†]
Kolesar, D. F.	

APPLIED PHYSICS

J. O. Dimmock, Leader
T. C. Harman, Assistant Leader
I. Melngailis, Assistant Leader

Butler, J. F.	Foyt, A. G.	Mooradian, A.
Calawa, A. R.	Halpern, J.	Oliver, M. [†]
Carter, F. B.	Hinkley, E. D.	Paladino, A. E.
Caswell, F. H.	Hurwitz, C. E.	Palermo, J. S.
Clough, T. F.	Lindley, W. T.	Phelan, R. J., Jr.
Donaldson, P. L.	McMullin, P. G. [†]	Quist, T. M.

Stella, J. A.	
Sullivan, F. M.	
Ward, J. H. R., III	
Wolfe, C. M.	
Youtz, P.	

* Part Time

† Summer Staff

‡ Research Assistant

§ Leave of Absence

REPORTS BY AUTHORS ENGAGED IN SOLID STATE RESEARCH

15 May through 15 August 1966

PUBLISHED REPORTS

Journal Articles*

JA No.

2613A	Automatic Potentiometric EDTA and Redox Titrations for Determinations of Stoichiometry	M. C. Gardels J. C. Cornwell	Anal. Chem. <u>38</u> , 774 (1966)
2633	A Note Concerning the Temperature Profile Within a Thermo-magnetic Energy Converter	T. C. Harman J. M. Honig	Adv. Energy Conversion <u>6</u> , 127 (1966)
2672	Pseudobinary InSb-InTe System	A. J. Strauss M. D. Banus M. C. Finn	J. Electrochem. Soc. <u>113</u> , 458 (1966)
2698	Structure of Equations Specifying Operating Characteristics of Energy Converters Constructed of Anisotropic Materials	J. M. Honig T. C. Harman	Adv. Energy Conversion <u>6</u> , 149 (1966)
2762	Electron-Bombardment Technique for Deposition of CdS Film Transducers	R. Weber	Rev. Sci. Instr. <u>37</u> , 955 (1966)
2776	Efficient Visible Lasers of $\text{CdS}_x\text{Se}_{1-x}$ by Electron-Beam Excitation	C. E. Hurwitz	Appl. Phys. Letters <u>8</u> , 243 (1966)
2794	High-Temperature Expansions - The Classical Heisenberg Model	H. E. Stanley T. A. Kaplan	Phys. Rev. Letters <u>16</u> , 981 (1966)
2802	Observation of the Interaction of Plasmons with Longitudinal Optical Phonons in GaAs	A. Mooradian G. B. Wright	Phys. Rev. Letters <u>16</u> , 999 (1966)
2806	Laser Properties of a Vapor-Grown Ruby	J. R. O'Connor P. S. Schaffer† R. A. Bradbury†	Appl. Phys. Letters <u>8</u> , 336 (1966)
2816	Band Structure and Laser Action in $\text{Pb}_x\text{Sn}_{1-x}\text{Te}$	J. O. Dimmock I. Melngailis A. J. Strauss	Phys. Rev. Letters <u>16</u> , 1193 (1966)

* Reprints available.

† Author not at Lincoln Laboratory.

JA No.

2822	Electroreflectance in Metals	J. Feinleib	Phys. Rev. Letters <u>16</u> , 1200 (1966)
MS-1294	Energy Band Parameter Determination in Graphite	M. S. Dresselhaus J. G. Mavroides	Carbon <u>3</u> , 465 (1966)

* * * *

UNPUBLISHED REPORTS

Journal Articles

JA No.

2723	Single Crystal Growth and Electrical Transport Properties of Intermediates in the Spinel System $\text{Co}_{1+\delta}\text{V}_{2-\delta}\text{O}_4$	D. B. Rogers* A. Ferretti W. Kunemann	Accepted by J. Phys. Chem. Solids
2725A	On the Thermodynamic Aspects of the Temperature-Pressure Phase Diagram of InTe	M. D. Banus P. M. Robinson*	Accepted by J. Appl. Phys.
2768	Anomaly in the X-Ray Scattering of ZnSe	P. M. Raccah R. J. Arnott A. Wold*	Accepted by Phys. Rev.
2774	Generalization of the RKKY Interaction for Nonspherical Fermi Surfaces	L. M. Roth* H. J. Zeiger T. A. Kaplan	Accepted by Phys. Rev.
2824	Incoherent Source Optical Pumping of Visible and Infrared Semiconductor Lasers	R. J. Phelan, Jr.	Accepted by Proc. IEEE
2827	Efficient Ultraviolet Laser Emission in Electron Beam Excited ZnS	C. E. Hurwitz	Accepted by Appl. Phys. Letters
2832	First Order Raman Effect in III-V Compounds	A. Mooradian G. B. Wright	Accepted by Solid State Commun.
2852	High Pressure Synthesis of Arsenopyrite-Type Ternary Compounds	M. D. Banus M. C. Lavine	Accepted by Materials Res. Bull.
MS-1577	Single Crystal Growth and Electrical Transport Properties of the Spinel MgV_2O_4	A. Ferretti D. B. Rogers*	Accepted by J. Phys. Chem. Solids

* Author not at Lincoln Laboratory.

Reports

Meeting Speeches*

MS No.

1520A	Self-Focusing of Optical Beams	P. L. Kelley	Bell Telephone Laboratories, Murray Hill, New Jersey. 14 July 1966
1571	Atomic Point Defects in Semiconductors	R. F. Brebrick	AIME, New England Regional Conference, Boston. 12-13 May 1966
1577	Single Crystal Growth and Electrical Transport Properties of the Spinel MgV_2O_4	A. Ferretti * D. B. Rogers *	International Conference on Crystal Growth, Boston. 20-24 June 1966
1578 A-D	Magnetoplasma Cyclotron Resonance in PbSe	S. Bermon	Michigan State University, 5 May 1966; Case Institute of Technology, 16 May 1966; Carnegie Institute, 17 May 1966; University of Maryland, 19 May 1966
1614	Spark Source Mass Spectroscopy	E. B. Owens	Fifth National Meeting, Society for Applied Spectroscopy, Chicago, Illinois, 13-17 June 1966
1627	Semiconductor Lasers	R. H. Rediker	IEEE Communications Conference, Philadelphia, Pennsylvania. 15-17 June 1966
1641	Intensity Fluctuations of Gas Lasers Below and Above the Threshold of Oscillations	C. Freed H. A. Haus†	Conference on Coherence and Quantum Optics, Rochester, New York, 22-25 June 1966
1675	Bulk GaAs Negative Conductance Amplifiers	A. G. Foyt A. L. McWhorter T. M. Quist	
1677	Small-Bandgap Semiconductor Infrared Lasers	I. Melngailis A. J. Strauss J. O. Dimmock	Solid-State Device Research Conference, Northwestern University, 15-17 June 1966
1693	Amplification at Subcritical Drift Velocities	A. L. McWhorter H. A. Haus†	
1706	Efficient Ultraviolet Laser in Electron Beam Excited ZnS	C. E. Hurwitz	
1676	Recent Work Concerning the Electrical Properties of Metal Oxides	J. M. Honig	National Bureau of Standards, Washington, D. C., 10 May 1966

* Titles of Meeting Speeches are listed for information only. No copies are available for distribution.

† Author not at Lincoln Laboratory.

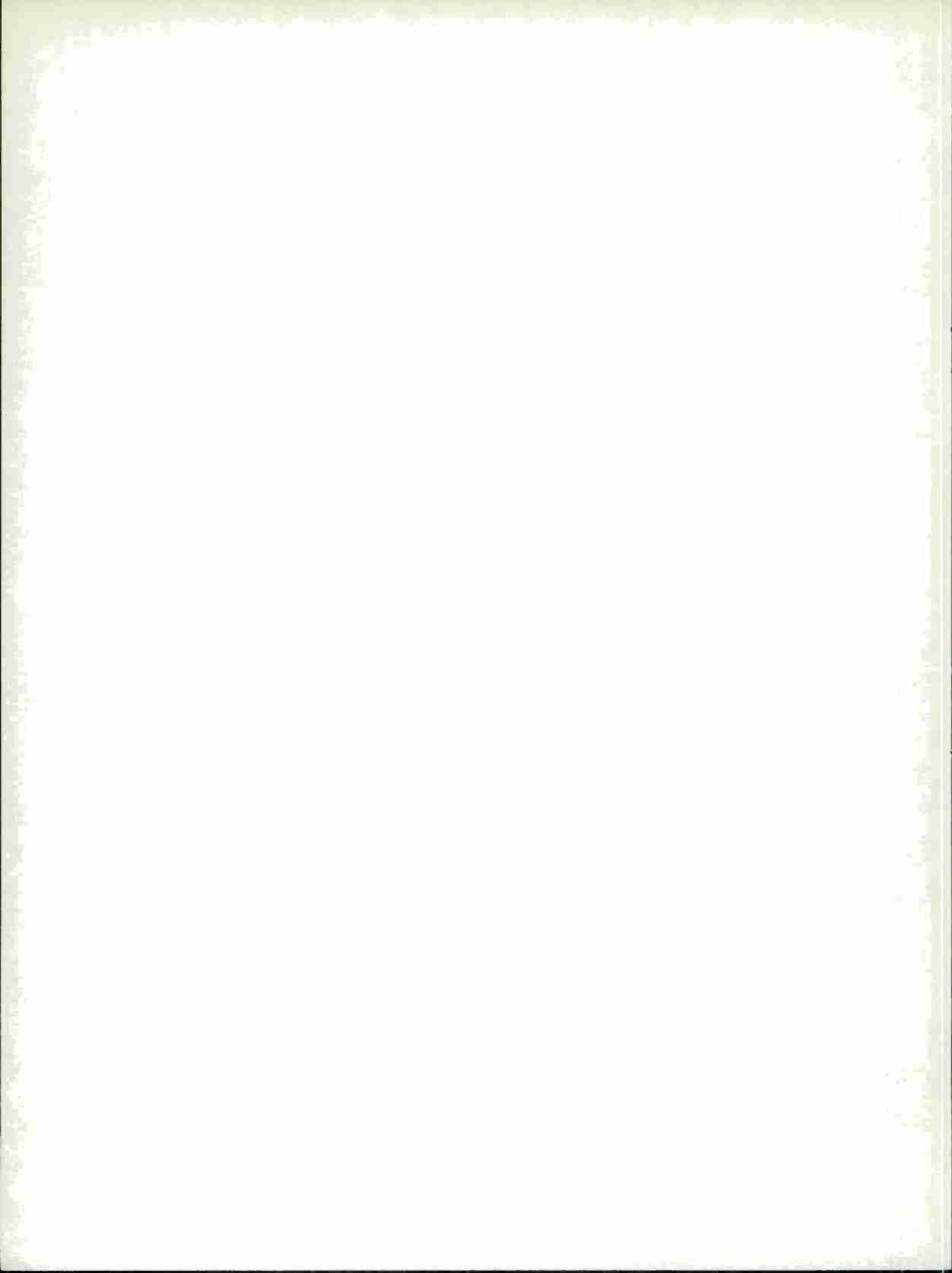
MS No.

1679	Polaron Induced Anomalies in InSb	E. J. Johnson	Rensselaer Polytechnic Institute, 19 May 1966
1707	Crystal Growth from the Vapor	S. Fischler	E.I. du Pont de Nemours & Co., Wilmington, Delaware, 17 June 1966
1712	Introduction to IV-VI Compounds	A. J. Strauss	Semiconductor Materials Meeting, New York, 24 June 1966
1721	Introduction to Nonlinear Optics and Self-Focusing of Light Beams	P. L. Kelley	Tutorial Lectures, Advances in Quantum Electronics Symposium, University of Colorado, 20 June – 1 July 1966
1722	Laser-Induced Gas Breakdown	M. M. Litvak	

ADDITIONAL UNPUBLISHED REPORTS

MS-1558	Possibility of Self-Focusing Due to Intensity Dependent Anomalous Dispersion	A. Javan* P. L. Kelley	Accepted by IEEE J. Quant. Electron.
MS-1554	Spectroscopic Studies of Laser- Produced Hydrogen Plasma	D. F. Edwards* M. M. Litvak	Accepted by IEEE J. Quant. Electron.
JA-2652	Electron Recombination in Laser- Produced Hydrogen Plasma	M. M. Litvak D. F. Edwards*	Accepted by J. Appl. Phys.
JA-2847	A Maser Model for Interstellar OH Microwave Emission	M. M. Litvak A. L. McWhorter M. L. Meeks H. J. Zeiger	Accepted by Phys. Rev. Letters

* Author not at Lincoln Laboratory.



I. SOLID STATE DEVICE RESEARCH

A. BAND STRUCTURE AND LASER ACTION IN $\text{Pb}_x\text{Sn}_{1-x}\text{Te}$

Spontaneous and coherent emission at wavelengths between 11 and 16 μ has been observed in $\text{Pb}_x\text{Sn}_{1-x}\text{Te}$ alloys at 12°K, optically excited by radiation from a GaAs diode laser. A model of the band structure of the alloy system has been proposed to explain the composition dependence of the band gap and the change in sign of the temperature coefficient of the band gap between PbTe and SnTe.

In the photoluminescence experiments, a small crystal sample and the GaAs laser pump were mounted on a copper heat sink which was in contact with liquid helium.¹ The Fabry-Perot cavity was formed by two parallel faces of the sample which were perpendicular to the surface irradiated by the GaAs laser beam. Current pulses of a few microseconds duration were applied to the GaAs diode at the rate of 3000/sec.

Figure I-1 shows the emission spectra of a $\text{Pb}_{0.81}\text{Sn}_{0.19}\text{Te}$ laser at 12°K, below and above threshold. The sample was a vapor-grown n-type crystal ($n = 1.7 \times 10^{17} \text{ cm}^{-3}$ at 77°K) with the as-grown shape of a parallelepiped 550 μ long in the direction of laser emission. The onset of coherent emission occurred at a GaAs diode current of 3.7 A, which corresponds to approximately 1.5 W of 0.84- μ radiation. A single-cavity mode at 15.9 μ was excited at currents between 3.7 and 8 A, and multimode operation was observed at higher currents. The mode spacing corresponds to a value of approximately 6.5 for quantity $[n_0 - \lambda_0 dn/d\lambda]$. Coherent emission was also obtained from a $\text{Pb}_{0.83}\text{Sn}_{0.17}\text{Te}$ alloy sample at 14.9 μ and from $\text{Pb}_{0.86}\text{Sn}_{0.14}\text{Te}$ at 11.6 μ .

The luminescence data of Fig. I-1 give an energy gap of 0.078 eV for $\text{Pb}_{0.81}\text{Sn}_{0.19}\text{Te}$ at 12°K, compared to 0.186 eV obtained in PbTe from luminescence measurements at this temperature.²

A decrease of the energy gap with increase in Sn concentration has also been observed in Pb-rich $\text{Pb}_x\text{Sn}_{1-x}\text{Te}$ alloys at 300°K by means of optical absorption measurements.^{3,4} However, recent tunneling experiments⁵ have indicated that SnTe is a semiconductor with an energy gap at 4.2°K of approximately 0.3 eV, that is, larger than the energy gap of either PbTe or $\text{Pb}_{0.81}\text{Sn}_{0.19}\text{Te}$ at low temperatures. Furthermore, inspection of the tunneling data at 300°K indicates that the band gap in SnTe at this temperature is approximately 0.18 eV, that is, smaller than the gap in SnTe at low temperatures. This decrease in the energy gap with increasing temperature is opposite to the temperature dependence of the energy gap in PbTe. These results led us to propose a band structure model of the $\text{Pb}_x\text{Sn}_{1-x}\text{Te}$ alloys in which the valence and conduction bands of SnTe are inverted from those of PbTe.

The valence and conduction band edges in PbTe occur at the L point in the Brillouin zone. It is believed that the valence band edge is an L_6^+ state and the conduction band edge is an L_6^- state.⁶ According to our proposed band model, with increasing Sn composition the energy gap initially decreases, goes to zero at some intermediate composition where the L_6^+ and L_6^- states become degenerate, and then increases, with the L_6^+ state now forming the conduction band edge and the L_6^- state forming the valence band edge. Since the L_6^+ and L_6^- states each have only a twofold spin degeneracy, their crossover does not result in a semimetal but in a semiconductor with the valence and conduction bands interchanged. Figure I-2 shows schematically the proposed

Section I

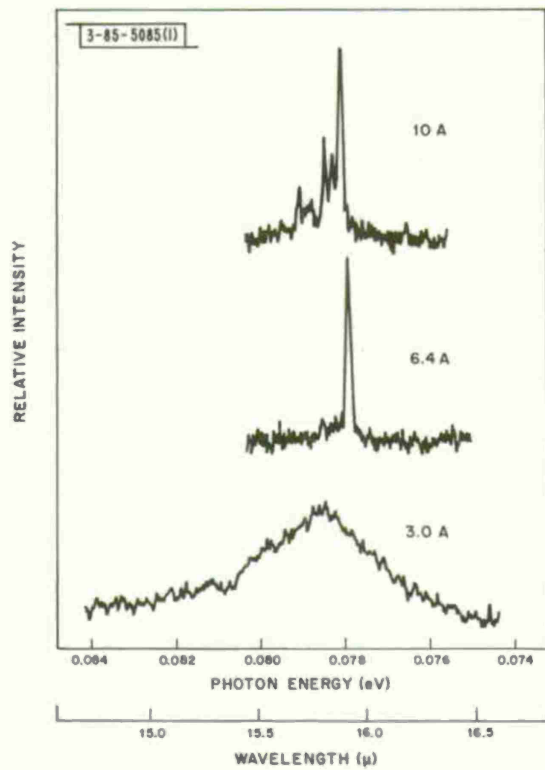


Fig. I-1. Emission spectra of optically excited $\text{Pb}_{0.81}\text{Sn}_{0.19}\text{Te}$ at about 12°K, obtained below threshold at GaAs diode current of 3 A and above threshold at 6.4 and 10 A. Spectra above threshold show resolution-limited mode structure.

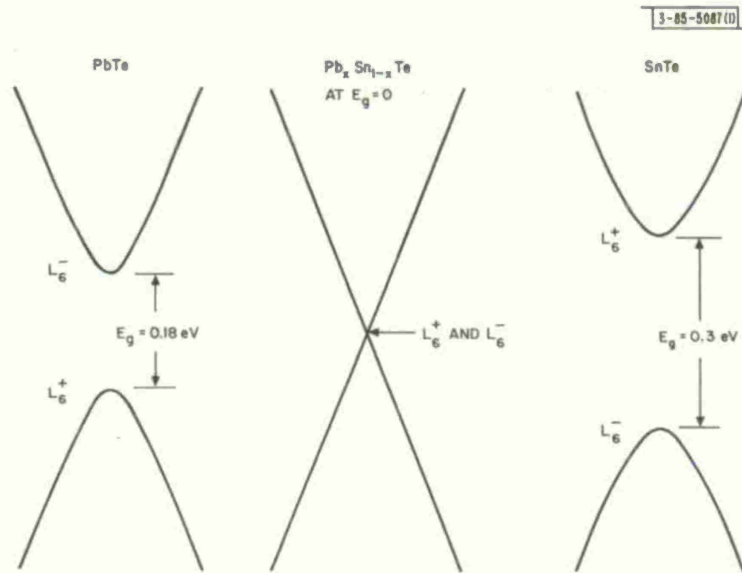


Fig. I-2. Schematic representation of valence and conduction bands at 12°K for PbTe, for the composition at which the energy gap is zero, and for SnTe.

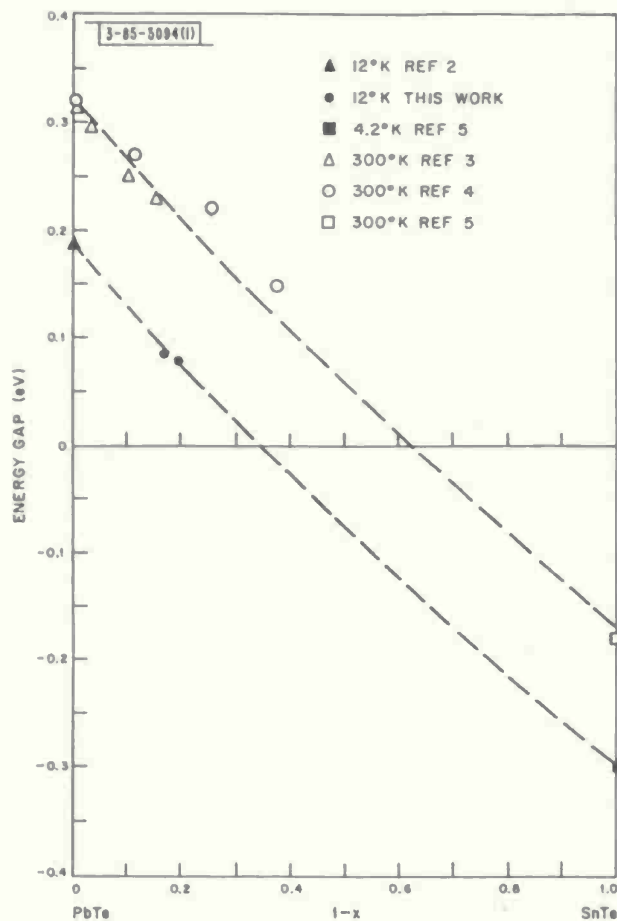


Fig. I-3. Energy gap of $\text{Pb}_x\text{Sn}_{1-x}\text{Te}$ as a function of mole fraction of SnTe, $1 - x$. Data points are obtained from luminescence at 12°K, optical absorption at 300°K, and tunneling in SnTe at 4.2° and 300°K.

model for valence and conduction bands for PbTe, for the composition at which the energy gap is zero, and for SnTe.

In Fig. I-3, we have plotted the energy gap as determined by the luminescence data at low temperatures and by the optical absorption data at 300°K. The gap energies determined from the tunneling experiments in SnTe are also plotted but as negative values to conform with the proposed inverted band model. A dashed curve has been drawn through the low temperature data to indicate roughly the gap variation with composition, and a parallel curve has been drawn through the room temperature data. The extrapolations indicate that at 12°K the energy gap passes through zero at $1 - x \approx 0.35$ whereas at 300°K this occurs at $1 - x \approx 0.62$.

The change in energy gap with composition for the $\text{Pb}_x\text{Sn}_{1-x}\text{Te}$ alloy series can be understood qualitatively in terms of the difference between the relativistic effects in Pb and Sn. Conklin, Johnson and Pratt⁶ have calculated the band structure of PbTe and have shown that relativistic corrections are extremely important in determining the positions of the energy bands. An estimate of the difference in these corrections for the conduction and valence bands of PbTe and SnTe can be obtained from the calculated band functions of PbTe and the difference in the relativistic effects for the valence states of atomic Pb and Sn. The band calculations indicate

Section I

that about 36 percent of the valence band L_6^+ state comes from a Pb s-state and 31 percent of the conduction band L_6^- state comes from a Pb p-state. The difference between the relativistic shifts of the valence states of Pb and Sn is 2.75 eV for the s-states (6s for Pb vs 5s for Sn) and 0.73 eV for the p-states.⁷ Using these values, we estimate an upward shift of the L_6^+ state by 0.99 eV and of the L_6^- state by 0.23 in going from PbTe to SnTe. This corresponds to a relative shift of 0.76 eV and indicates that the bands should cross at some intermediate value of composition. The data and interpretation indicated in Fig. I-3 call for a shift of only about 0.5 eV. Relativistic effects, therefore, more than account for the change in energy gap required by the model. On the basis of the difference between the relativistic shifts in Pb and Sn, similar variations in band structure with composition can be expected in the $Pb_xSn_{1-x}Se$ and $Pb_xSn_{1-x}S$ alloys with rock-salt structure.

Because of the energy band crossover, the temperature dependence of the energy gap for SnTe and the Sn-rich alloys is of opposite sign and, as can be seen from the data in Fig. I-3, about equal in magnitude to that of PbTe and the Pb-rich alloys. This should be true for the pressure dependence of the energy gap as well. For alloys on the Sn-rich side of $Pb_{0.65}Sn_{0.35}Te$, it should be possible to close the energy gap by increasing the temperature. For alloys on the Pb-rich side, it should be possible to close the energy gap by increasing the pressure. The energy gap in SnTe should close at about 470°C, whereas at 12°K the energy gap in PbTe should close at about 25 kbar.⁸ For the alloy $Pb_{0.81}Sn_{0.19}Te$, the energy gap at 12°K should close at about 10 kbar, assuming that the pressure coefficient is the same as that of PbTe. The possibility of arbitrarily reducing the energy gap by changing the composition or by varying pressure or temperature is especially attractive for use in long wavelength infrared detection as well as for tunable long wavelength lasers. Unfortunately, many of the interesting transport phenomena associated with small effective masses may be obscured in the $Pb_xSn_{1-x}Te$ alloys because at present they can be grown only with very high carrier concentrations. However, it should be interesting to observe the luminescence as the gap energy approaches the vicinity of the optical phonon energies. This occurs at 0.0135 eV or 92 μ (longitudinal) or 0.0039 eV or 320 μ (transverse) in PbTe.⁹ One would expect the luminescence to be quenched in the vicinity of these energies due to the possibility of nonradiative interband transitions via optical phonons. On the other hand, this may result in the generation of unusually high optical phonon densities. If quenching does occur, it would also be interesting to see if the luminescence resumes at longer wavelengths and, if so, at what wavelength it finally ceases.

J. O. Dimmock
I. Melngailis
A. J. Strauss

B. EFFICIENT ULTRAVIOLET LASER EMISSION IN ELECTRON BEAM EXCITED ZnS*

Using pulsed electron beam excitation on single crystals of ZnS, we have obtained at both liquid helium and nitrogen temperatures efficient semiconductor lasers in the ultraviolet portion of the spectrum. Up to 1.7 W of peak output power with a power efficiency of 6.5 percent has been measured in the spectral range from 3245 to 3300 Å. Efficient electron-beam-pumped laser

* The work described in this section was supported in part by the AF Avionics Laboratory Director's Fund, Item Nr. 65-86.

emission^{10,11} in the visible region from crystals of CdS, CdSe, and CdS_xSe_{1-x} and ultraviolet laser emission¹² with substantially lower efficiency from ZnO have recently been reported.

Laser samples were made from undoped, single-crystal, vapor-grown platelets of hexagonal ZnS. The sample preparation and experimental techniques have been described previously.¹⁰ Sample dimensions were approximately 150 μ × 2-3 μ × 1 mm, the first dimension being that of the optical cavity. In addition to the strong ultraviolet fluorescence, the samples exhibited some very faint yellow emission. However, none of the well-known red, green, or blue fluorescence found in ZnS phosphors was detected, indicating that these crystals were essentially free of the deep impurities responsible for this visible emission. The electron beam of approximately 0.5-mm diameter was pulsed with 200-nsec pulses at a repetition rate of 60/sec.

Typical spectra at liquid helium temperature slightly below and above the laser threshold are shown in Fig. I-4. The abrupt appearance of the strong laser line at 3291 Å is clearly evident. Actually, this line is only one of at least 10 laser lines which were observed to be

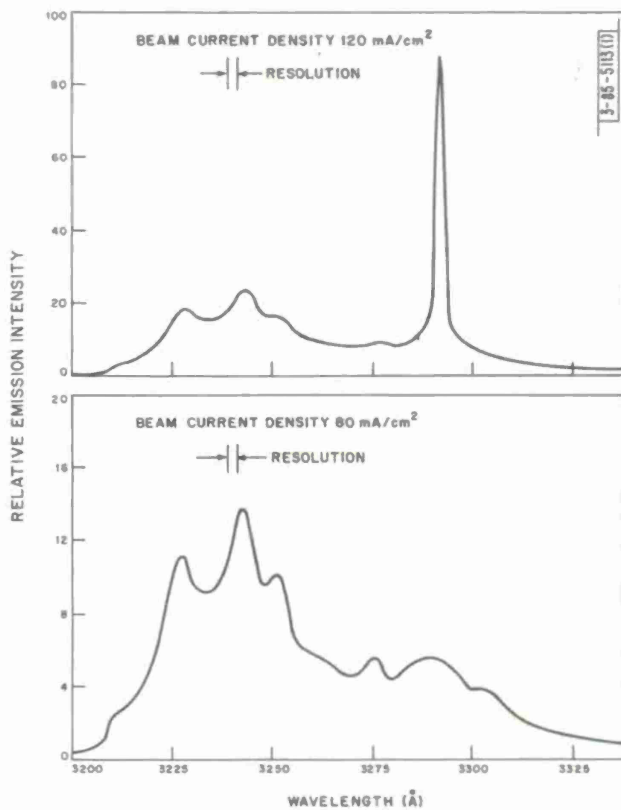


Fig. I-4. Emission spectra of electron-beam-pumped ZnS near liquid helium temperature: below laser threshold (lower trace) and slightly above laser threshold (upper trace). Electron energy is 40 keV. Sample dimensions are 150 μ × 3 μ × 1 mm; first dimension is cavity length. Note difference in emission intensity scales.

Section I

emanating from a single sample at irregularly spaced wavelength intervals in the region from 3245 to 3300 Å. The threshold current densities for these lines varied somewhat, but did not appear to be correlated with the emission wavelengths. By carefully focusing a magnified (2:1) image of the emitting face of the sample at the plane of the entrance slit of the spectrometer, and then scanning this image across the slit opening, it was determined that these laser lines were being emitted from different points on the cavity face. Each line presumably corresponds to a different laser filament, and the spatial variation in wavelength is most probably caused by crystal inhomogeneities (e.g., variations in impurity or defect concentrations). Within the estimated 50-μ spatial resolution of the optical system, there was no corresponding variation in the spontaneous emission spectrum. The significance of this latter observation is obscured somewhat by the fact that the effective spatial resolution for the laser emission is much finer, being approximately equal to the 2.5-μ filament diameter, the value of which was inferred from the measured 7° beam angle for single filament emission. Similar results were obtained at nitrogen temperature, with the lines shifted about 15 Å toward longer wavelengths, in accordance with the decrease of the energy gap at the higher temperature. Further work is now in progress in an attempt to understand the observed behavior.

Although the free exciton transitions occurring at wavelengths of 3200 Å and shorter have been identified,¹³ the published studies of the optical properties of hexagonal ZnS in the spectral region from 3200 to 3300 Å lack sufficient detail and general agreement to permit the identification of the optical transitions involved in the present spontaneous and stimulated emission. However, in analogy with CdS, the major spontaneous peaks are probably related to bound exciton states.^{14,15} We note that, as in CdS, both the spontaneous and stimulated emission were strongly polarized with $E \perp C$.

With high spectral resolution, each of the laser lines exhibits the familiar Fabry-Perot cavity mode structure, a typical example of which is shown in Fig. I-5 for the 3291 Å line. A

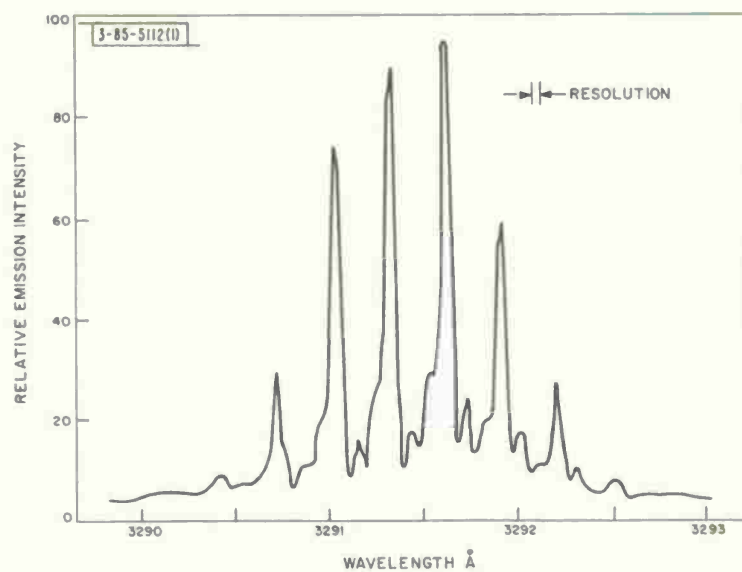


Fig. I-5. High resolution spectrum of 3291 Å laser line from electron-beam-pumped ZnS near liquid helium temperature. Electron energy is 40 keV and beam current density is 1.6 A/cm². Sample dimensions are same as for Fig. I-4.

time-resolved spectroscopic technique¹⁰ was employed to minimize the spectral shift and consequent blurring of the modes due to the rise in sample temperature during the pulse. No other significant temporal changes in the laser spectra were observed. Because of the very large dispersion of the refractive index of ZnS near the energy gap,¹⁶ the mode spacing decreases monotonically with decreasing wavelength, from a value of 0.3 Å at 3291 Å to 0.16 Å at 3245 Å. Using the usual Fabry-Perot mode spacing formula, including the dispersion correction, and a measured cavity length of 150 μ, the above spacings correspond to values for $[n_0 - \lambda_0 dn/d\lambda]$ of 12 at 3291 Å and 22 at 3245 Å.

The minimum electron energies for laser action were 18 keV at helium temperature and 26 keV at nitrogen temperature, for which the threshold current densities were about 750 and 400 mA/cm², respectively. The threshold current decreased rapidly with increasing electron energy, but began to level off as the energy reached about 40 keV, at which point a significant fraction of the incident electrons began to pass completely through the thin samples. At 40 keV, the threshold current densities were approximately 100 and 400 mA/cm² at helium and nitrogen temperatures, respectively.

The peak output power and efficiency increased strongly with both beam voltage and current but began to saturate at a voltage of 40 kV due to the loss of fast electrons through the sample, and high currents due to heating. A peak output power of 1.7 W with a corresponding power efficiency of 6.5 percent at helium temperature and 0.6 W with an efficiency of 2 percent at nitrogen temperature was measured.

By analogy with the results¹¹ in CdS_xSe_{1-x}, this observation of efficient laser action in ZnS indicates that it also should be possible to produce efficient lasers of the ternary compound Zn_xCd_{1-x}S, thus extending to 3245 Å the continuous wavelength range of efficient semiconductor lasers.

C. E. Hurwitz

C. ELECTRON BEAM PUMPED LASERS OF ZnO AND CdS

The observation of laser action near 3750 Å in ZnO excited by a 15-keV electron beam was first reported by Nicoll.¹² Using a beam with electron energies up to 50 keV, we have obtained ZnO lasers with almost an order of magnitude lower threshold currents and with higher power conversion efficiencies than those observed by Nicoll. Sample dimensions were approximately 250 μ × 5 μ × 1 mm and the beam was pulsed with 200-nsec pulses at a repetition rate of 60/sec. With a 50-keV beam the threshold current density at both liquid helium and liquid nitrogen temperatures was about 200 mA/cm². A peak output power of 1 W with an efficiency of 1.3 percent at 4.2°K and 0.5 W with an efficiency of 0.5 percent at 77°K was measured.

Previous measurements on CdS electron beam pumped lasers^{10,11} consistently yielded higher values for the threshold currents and lower values for the power efficiencies than obtained for CdSe and for CdS_xSe_{1-x}, with x as large as 0.9. Using some new CdS platelets received from D. C. Reynolds of the Aerospace Research Laboratory, Wright-Patterson AFB, we have now obtained CdS electron beam pumped lasers with thresholds and efficiencies more nearly in line with those obtained in the other II-VI semiconductor lasers. For a 50-keV beam, threshold current densities as low as 200 mA/cm² at 4.2°K and 400 mA/cm² at 77°K and efficiencies as high as 7 and 1.5 percent respectively, have been measured. The particular crystal property

Section I

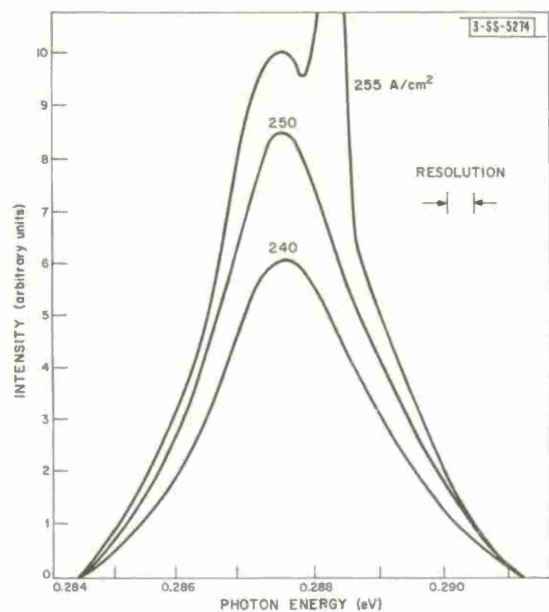


Fig. I-6. Emission spectra for PbS diode laser at approximately 10°K.

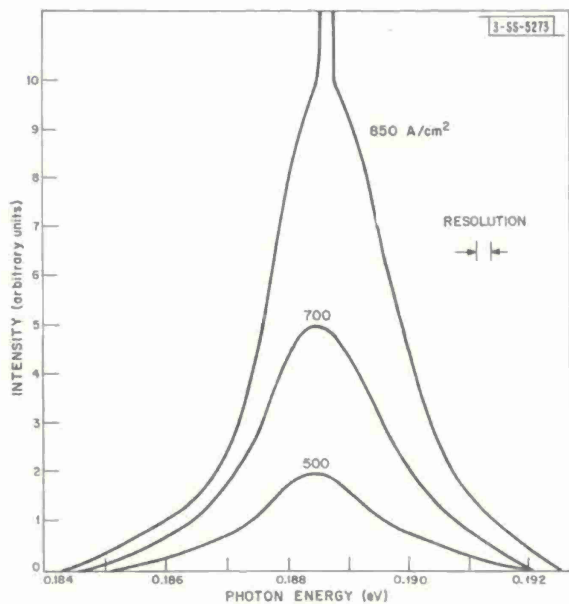


Fig. I-7. Emission spectra for PbTe diode laser at approximately 7°K.

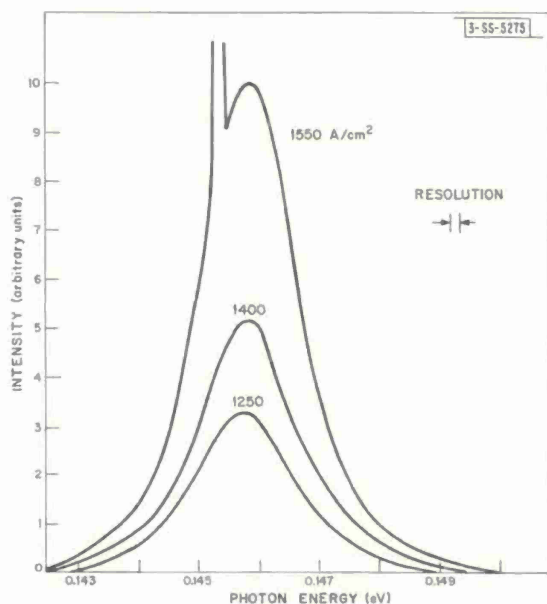


Fig. I-8. Emission spectra for PbSe diode laser at approximately 7°K.

whose variation gives rise to large observed variations in efficiency and threshold is unknown; however, further investigation of this behavior is presently underway.

C. E. Hurwitz

D. FLASHLAMP PUMPING OF SEMICONDUCTOR LASERS

Xenon flashlamp pumping of semiconductor lasers was extended to shorter wavelengths and higher temperatures. The lowest thresholds obtained and the emission wavelengths are given in Table I-1 for the semiconductors studied. For each of these samples the cavity length was about 500μ . In order to compare the results with those to be expected in electrical injection devices, the thresholds have been expressed in equivalent kA/cm^2 by multiplying the photon flux density by the electron charge. Only the pump photons with wavelengths shorter than the emission wavelengths were considered. Multiple electron-hole pair production and reflection losses were neglected. Computing the equivalent electron-hole pair production from the electron beam results of Hurwitz¹⁷ on $\text{CdS}_x\text{Se}_{1-x}$ using the approximations of Klein,¹⁸ one obtains thresholds in this same region. This agreement between the thresholds for optical and electron beam pumping implies that the active volumes were similar. Additionally, the laser thresholds of optically pumped InSb and diodes made of this material are in agreement. One may conclude that devices such as p-n junctions of these II-VI semiconductors, not yet fabricated, may be expected to have laser thresholds comparable to those given in Table I-1.

TABLE I-1
OPTICALLY PUMPED LASER THRESHOLD VALUES AND LASER EMISSION WAVELENGTHS.
THE THRESHOLD VALUES HAVE BEEN EXPRESSED AS AN EQUIVALENT CURRENT DENSITY
BY MULTIPLYING THE PHOTON FLUX DENSITY BY THE ELECTRON CHARGE

Material	Temperature (°K)	Flux Density (kA/cm^2)	Wavelength (μ)
InSb	4	0.3	5.3
CdSe	4	0.8	0.685
	77	1.5	0.699
$\text{CdS}_{0.6}\text{Se}_{0.4}$	4	1.7	0.560
	77	6.2	0.567
CdS	4	3.9	0.493
	77	5.5	0.497

R. J. Phelan, Jr.

E. EMISSION SPECTRA OF Pb SALT DIODE LASERS

Figures I-6 through I-8 show the emission spectra measured at several injection levels for diode lasers of PbS, PbTe, and PbSe. The diodes were fabricated from p-type annealed material

Section I

with carrier concentrations of $3 \times 10^{17} \text{ cm}^{-3}$ for PbS, $6.5 \times 10^{17} \text{ cm}^{-3}$ for PbTe and $2 \times 10^{17} \text{ cm}^{-3}$ for PbSe. Fabrication methods and spectral measuring techniques have been previously described.¹⁹⁻²¹ In these devices the four cleaved sides perpendicular to the p-n junction plane act as totally reflecting surfaces and laser action probably occurs in the internally reflected modes of the rectangular cavity. In all spectral measurements, the light path outside the dewars was maintained in a dry nitrogen atmosphere. Diode currents were supplied in pulses of a few microseconds duration at a repetition rate of 10 kc/sec. Threshold currents for the PbTe and PbSe diodes used in these experiments were substantially higher than in previously investigated units.

The emission spectra for the three materials are qualitatively similar to each other. Note that laser action is seen initially as an abrupt spike; there is no narrowing of the overall spectrum. This property seems to be characteristic of diodes in which laser action occurs in totally reflected internal modes and has been observed in other semiconductors.²² Spontaneous emission linewidths are 2.7, 2.3 and 1.8 meV for PbS, PbTe and PbSe, respectively. The shapes of the spontaneous emission curves remain unchanged with increasing injection level. A small shift to higher energies presumably due to heating, which is especially noticeable in Fig. I-7, could be decreased by lowering the diode current duty cycle. The energy difference between the spontaneous peaks of the 500 and 850 A/cm^2 spectra in Fig. I-7 corresponds to a temperature rise of about 0.5°K .

A detailed analysis of these spectra is felt to be inappropriate because of lack of knowledge of distributions of donors and acceptors near the p-n junctions and because of the difficulty in accounting realistically for distortion of the spectra by self-absorption. However, some qualitative observations can be made. The invariance of spectral shapes and peak positions with increasing diode current implies an absence of band filling and suggests that injected carriers are nondegenerate, even at laser threshold. The spectral widths are consistent with radiative transitions being predominantly between bands. This is the expected model for radiative transitions in the Pb salts since, due to the large static dielectric constants,^{23,24,25} shallow impurity and exciton binding energies are negligible. Magnetic field studies²⁶ give further evidence that luminescence is due to band-to-band transitions. The low energy tails evident on all spectra may be attributed to transitions in which \mathbf{k} is not conserved, or to spatial variations in the energy gaps caused by lattice distortions in the vicinity of impurities or other lattice defects.

Emission peaks have been observed about 27, 23 and 15 meV below the main emission peaks of PbS, PbTe and PbSe, respectively. In each material the spectral shape and intensity of this low energy emission varied from one diode to another and, in many units, were absent. This variability suggests that it is associated with impurities.

J. F. Butler

REFERENCES

1. For details of the experimental arrangements, see R. J. Phelan, Jr. and R. H. Rediker, *Appl. Phys. Letters* 6, 70 (1965).
2. J. F. Butler and A. R. Calawa, Physics of Quantum Electronics (McGraw-Hill, New York, 1966), p. 458. The results of this paper show that the emission wavelength of the Pb salts corresponds to the energy gap.
3. P. M. Nikolic, *Brit. J. Appl. Phys.* 16, 1075 (1965). Also P. M. Nikolic and J. C. Woolley, private communication.
4. E. G. Bylander, Materials Science and Engineering (to be published).
5. L. Esaki and P. J. Stiles, *Phys. Rev. Letters* (to be published).
6. J. B. Conklin, Jr., L. E. Johnson, and G. W. Pratt, Jr., *Phys. Rev.* 137, A1282 (1965).
7. F. Herman and S. Skillman, Atomic Structure Calculations (Prentice-Hall, N. J., 1963).
8. Obtained using a pressure coefficient of the energy gap in PbTe of $-7.5 \pm 0.3 \times 10^{-6}$ eV/Bar (V. Prakash and W. Paul, private communication).
9. E. G. Bylander and M. Hass, *Solid State Commun.* 4, 51 (1966).
10. C. E. Hurwitz, *Appl. Phys. Letters* 8, 121 (1966).
11. _____, *Appl. Phys. Letters* 8, 243 (1966).
12. F. H. Nicoll, *Appl. Phys. Letters* 9, 13 (1966).
13. R. G. Wheeler and J. C. Mikloz, Proceedings of the 7th International Conference on Semiconductors, (Dunod, Paris, 1964) p. 873.
14. D. G. Thomas and J. J. Hopfield, *Phys. Rev.* 128, 2135 (1962).
15. D. C. Reynolds, C. W. Litton and T. C. Collins, *Phys. Stat. Sol.* 9, 645 (1965); 12, 3 (1965).
16. T. M. Bieniewski and S. J. Czyzak, *J. Opt. Soc. Am.* 53, 496 (1963). These data were taken at 298°K, but show the large dispersion of the refractive index in ZnS.
17. C. E. Hurwitz, *Appl. Physics Letters* 8, 243 (1966).
18. C. A. Klein, Physics of Quantum Electronics (McGraw-Hill, New York, 1966) p. 424.
19. J. F. Butler and A. R. Calawa, *J. Electrochem. Soc.* 112, 1056 (1965).
20. J. F. Butler, A. R. Calawa, R. J. Phelan, Jr., T. C. Harman, A. J. Strauss and R. H. Rediker, *Appl. Phys. Letters* 5, 75 (1964).
21. J. F. Butler, A. R. Calawa, and R. H. Rediker, *IEEE J. Quantum Electronics* 1, 4 (1965).
22. G. Burns and M. I. Nathan, *Proc. IEEE* 52, 770 (1964).
23. J. Zemel, Proceedings of the 7th International Conference on Semiconductors, (Dunod, Paris, 1964) p. 1061.
24. W. Cochran, *Phys. Letters* 13, 193 (1964).
25. E. Burstein, R. Wheeler and J. Zemel, Proceedings of the 7th International Conference on Semiconductors, (Dunod, Paris, 1964) p. 1065.
26. J. F. Butler and A. R. Calawa, Physics of Quantum Electronics, (McGraw-Hill, New York, 1966) p. 458.



II. OPTICAL TECHNIQUES AND DEVICES

A. ELECTRO-OPTIC EFFECT IN TRIGONAL SELENIUM AT 10.6 μm

Recent interest in the nonlinear optical behavior of selenium in the infrared^{1,2} has led us to consider its electro-optic properties in this region. We have observed the electro-optic effect in crystalline selenium (32 point-group symmetry) for 10.6- μm radiation, and measured its value to be $r_{11} \sim 2.5 \times 10^{10} \text{ cm/V}$. Trigonal selenium, which is a member of group VIB of the periodic table, is an elemental semiconductor with a bandgap at $\sim 8000 \text{ \AA}$. It is uniaxial and piezoelectric, and appears to be the first elemental crystal in which the electro-optic effect has been observed. As expected from its large index of refraction,³ the electro-optic coefficient of selenium was found to be relatively high (considering class 32 crystals, it is the highest observed to date).

The observed electro-optic coefficient is in agreement with Miller's phenomenological theory of optical harmonic generation, optical rectification, and linear electro-optic effect.⁴ Thus the tensor element discussed by Miller, calculated from the measured electro-optic coefficient r_{11} , has a value $\delta_{11}^{\omega}(\text{Se})/(4\pi)^3 \sim 0.1 \times 10^{-9} \text{ esu}$, which is comparable in size with the value for quartz which is $\delta_{11}^{\omega}(\text{quartz})/(4\pi)^3 \sim 0.25 \times 10^{-9} \text{ esu}$ (quartz is also a piezoelectric crystal of 32 point-group symmetry), as well as with the values for other crystals measured to date.⁴ Qualitative agreement of the kind discussed by Miller is also seen between the SHG tensor element for Se which is given by Patel² as $\delta_{11}^{2\omega}(\text{Se})/(4\pi)^3 \sim 0.5 \times 10^{-9} \text{ esu}$, and the value of $\delta_{11}^{\omega}(\text{Se})/(4\pi)^3$ given above.

M. C. Teich
Theodore Kaplan

B. RUBY LASER RADAR

A program is in progress to track and obtain accurate ranges of orbiting satellites through use of a combination of microwave and optical radar techniques. High-power pulsed lasers, such as Q-switched ruby, can emit very short and intense pulses having small beam divergence. Such beam intensities incident on satellites having cube-corner retroreflectors result in significant radiation intensities at a suitable receiver, permitting range determinations of the bodies to accuracies of a few centimeters. Because the laser beam divergence is typically about a milliradian, it is necessary to provide pointing of the laser mount onto the object to a minimum of such accuracy. With laser pulse repetition rates of about 1/sec, it is not practical to attempt to acquire or hold an orbiting body in the laser's field of view by using laser "echoes" alone. It is very possible to use manual optical tracking techniques during the hours that a sunlit satellite is viewed against a darkened sky, but this restricts observation periods to orbits in view shortly after sunset and also shortly before sunrise. Such limitations are removed if the acquisition and pointing is done by slaving the laser's mount to a microwave radar that is tracking the satellite.

A ruby laser has been mounted on a modified Nike-Ajax antenna mount which has been interconnected with Lincoln Laboratory's Millstone Hill radar in Westford, Massachusetts. The laser mount has been placed atop a 40-foot tower located about 300 feet from the radar antenna, and

Section II

provision has been made for matching its position servos with those of the radar antenna. Tracking accuracy of this combination has been determined by observing the brightly illuminated satellites Echo I and Echo II on a television pickup which has been boresighted to the laser axis and has been found to be within 1 mrad as required.

The laser employed for this work has a 5/8 by 7-1/2 inch ruby rod with end faces cut at Brewster's angle. Linear flashlamps are mounted in a dual elliptical cavity with the ruby, and the optical resonator is formed by an uncoated quartz or sapphire plate at the front and a revolving rooftop prism at the rear. A saturable-dye cell is also used to sharpen the output pulse. Typical pulses are between 3 and 5 J with durations of about 20 nsec. Divergence of the outgoing laser beam is reduced by passing it through an 8-to-1 confocal recollimator. The pulse repetition rate of the laser is variable upward to 1/sec.

Reflected laser light has been collected by a 10-inch-diameter Cassegrainian telescope with a field of view of 6 mrad, passed through a 30-Å interference filter, and detected by a 10-stage photomultiplier tube. A fast discriminator circuit passes photomultiplier pulses which exceed a predetermined threshold level and rejects all others. A gate pulse is also provided to the discriminator in order that photomultiplier pulses be accepted only during periods when laser echoes are to be expected. The discriminator output is used to stop a time-interval counter which is initiated by the outgoing laser pulse. Time intervals may be resolved to 1 nsec with the unit being used.

Echoes from the satellite Explorer XXII have been obtained for satellite ranges varying between about 1000 and 580 nm. These were obtained during evening passes; however, a narrower bandpass filter is being installed so that daylight orbits may be observed. A 23-inch-diameter telescope is being installed in place of the 10-inch telescope already used. We expect that the combination of narrow-band filtering and the large-diameter telescope will permit observation of some "noncooperative" satellites at somewhat shorter ranges.

H. A. Bostick
P. R. Longaker

REFERENCES

1. C. K. N. Patel, Phys. Rev. Letters 15, 1027 (1965).
2. _____, Phys. Rev. Letters 16, 613 (1966).
3. R. S. Caldwell and H. Y. Fan, Phys. Rev. 114, 664 (1959).
Note that the value of n_e for selenium is misprinted in Ref. 2.
4. R. C. Miller, Appl. Phys. Letters 5, 17 (1964).

III. MATERIALS RESEARCH

A. HIGH-PRESSURE PHASES OF InSb

The existence of a new high-pressure phase of InSb, which we designated as InSb(III), was reported previously.¹ The superconducting transition temperature T_c for this phase is $4.05^\circ \pm 0.11^\circ\text{K}$ compared with $2.0^\circ \pm 0.1^\circ\text{K}$ for InSb(II), the high-pressure phase with tetragonal β -Sn structure. Measurements of T_c as a function of annealing pressure and temperature showed that with increasing temperature, InSb(II) is transformed into InSb(III) at $308^\circ \pm 7^\circ\text{C}$ for a pressure of 37 kbars, and at $287^\circ \pm 12^\circ\text{C}$ for 52 kbars.

Metal solution calorimetry² has now been used³ to determine the heat of formation of InSb(III) as well as the heats of formation of InSb(I), the atmospheric pressure phase, and of InSb(II). The results are given in Table III-1. The heats of transformation between the three phases, which were obtained by taking the differences between their heats of formation, are listed in Table III-2. All the heat values refer to 78°K , since it was necessary to keep the InSb(II) and InSb(III) samples at this temperature until dissolution in order to prevent transformation of these metastable phases into InSb(I). The measured heat of formation for InSb(I), $-3.560 \pm 0.045 \text{ kcal/g-atom}$, agrees well with the preliminary value of $3.58 \pm 0.11 \text{ kcal/g-atom}$ obtained by Robinson and Bever.⁴ The small positive value of the heat of transformation for $\text{InSb(II)} \rightarrow \text{InSb(III)}$ is consistent with the shallow negative slope of the boundary between these phases in the pressure vs temperature diagram (Fig. III-1).

The results of x-ray diffraction studies show that InSb(III) is not the same phase as the high-pressure orthorhombic InSb first obtained by Kasper and Brandhorst⁵ at room temperature. In one series of experiments, an MRC high-pressure camera with diamond anvils was used for measurements at high pressures and elevated temperatures. With the sample at room temperature, the pressure was first increased in steps until a diffraction pattern for single-phase InSb(II) was obtained at an estimated pressure of 40 to 50 kbars. (Because of large pressure gradients across the anvils, precise pressure values cannot be obtained with this apparatus.) The average pressure was then kept constant and measurements were made at temperature intervals of 50°C up to 300°C , where InSb(III) is the stable phase in this pressure range. Although the diffraction patterns are not good enough for a detailed structure determination, they show that a new phase

TABLE III-1
HEATS OF FORMATION FOR InSb PHASES AT 78°K

Reaction	Heat of Formation (kcal/g-atom)
$\text{In} + \text{Sb} \rightarrow \text{InSb(I)}$	-3.560 ± 0.045
$\text{In} + \text{Sb} \rightarrow \text{InSb(II)}$	-1.040 ± 0.060
$\text{In} + \text{Sb} \rightarrow \text{InSb(III)}$	-0.810 ± 0.060

Section III

TABLE III-2
HEATS OF TRANSFORMATION FOR InSb PHASES AT 78°K

Reaction	Heat of Transformation (kcal/g-atom)
InSb(I) \rightarrow InSb(II)	+2.520 \pm 0.055
InSb(I) \rightarrow InSb(III)	+2.750 \pm 0.055
InSb(II) \rightarrow InSb(III)	+0.230 \pm 0.070

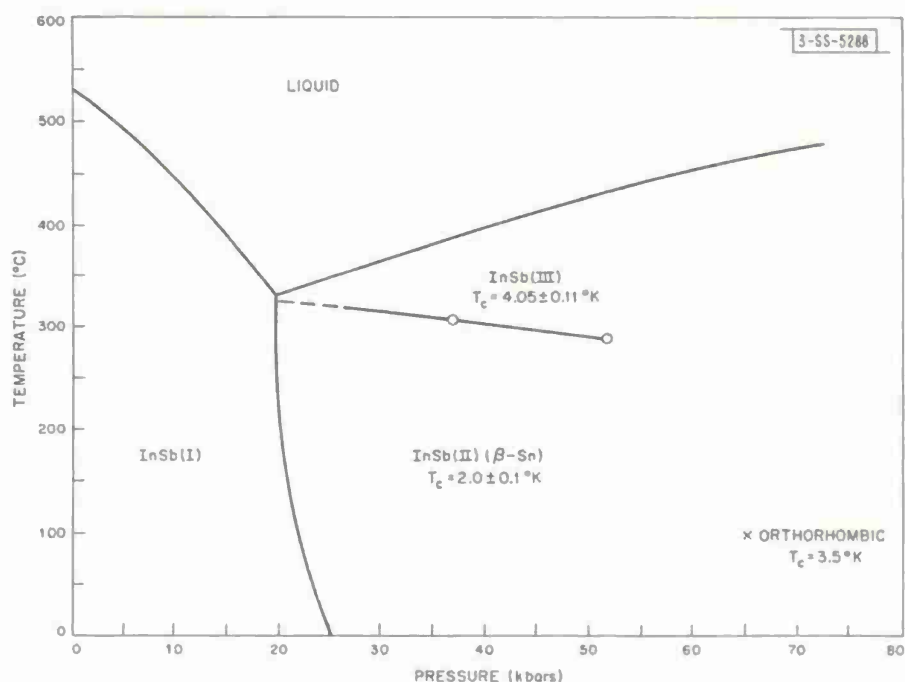


Fig. III-1. Pressure vs temperature for InSb.

which differs from orthorhombic InSb was obtained above 200°C. This new phase can be identified as InSb(III), since all the diffraction lines observed are also present in the diffraction patterns obtained for InSb(III) samples kept at 130° to 150°K and measured at atmospheric pressure with a Norelco diffractometer equipped with a low-temperature stage.

Superconductivity data also show that InSb(III) is different from the orthorhombic phase, since T_c is close to 4.0°K for InSb(III), while McWhan and Marezio⁶ found that T_c is about 3.4°K for the orthorhombic phase.

A partial pressure vs temperature diagram for InSb is given in Fig. III-1. In addition to the literature values for the liquidus lines and the InSb(I)-InSb(II) phase boundary, the diagram includes a portion of the phase boundary between InSb(II) and InSb(III), which is based on the data for 37 and 52 kbars reported previously.¹ Results currently available are not sufficiently reliable to establish any points on the boundaries between the orthorhombic phase and either InSb(II) or InSb(III). Thus the reported values for the pressure at which InSb(II) is transformed into the orthorhombic phase at room temperature range from 30 kbars (Ref. 5) to 80 kbars (Ref. 7). As indicated by a data point in Fig. III-1, a recent experiment showed that the orthorhombic phase is stable at 65 kbars and 100°C, since a T_c value of 3.55°K was observed for a sample annealed under these conditions for seven days without first being melted under pressure. However, for samples melted at 65 kbars and then annealed at this pressure for four days at 100° to 125°C, T_c was 4.0°K. Apparently the annealing time for these samples was not sufficient to transform them from the InSb(III) phase, which crystallized from the melt, to the orthorhombic phase stable under the annealing conditions. The slow rate at which InSb(III) retransforms under pressure was also apparent in an experiment with the high-pressure x-ray camera. In this case, a sample was transformed to InSb(III) by heating to 300°C at about 50 kbars and then cooled to room temperature without releasing the pressure. A diffraction pattern obtained after more than a week at room temperature showed that the sample still had the InSb(III) structure.

M. D. Banus A. Jena*
Mary C. Lavine M. B. Bever*

B. PRESSURE DEPENDENCE OF B8 = B31 TRANSITION TEMPERATURE IN MnAs

Under atmospheric pressure, MnAs is transformed at 317°K (44°C) from the low-temperature phase with B8 structure to the high-temperature B31 phase. It was reported previously⁸ that the transition temperature is decreased by application of hydrostatic pressure. On the basis of the pressure vs temperature relationship down to 200°K, the lowest temperature investigated, it was suggested that above a critical pressure of about 4.5 kbars, the B31 structure would be stable at all temperatures. This value for the critical pressure has now been confirmed by measuring the resistivity of MnAs as a function of pressure at 77°K. The experimental technique was essentially the same as described previously,⁹ except that an apparatus using helium gas as the pressure transmitting medium was substituted for the earlier apparatus, which uses liquid isopentane. The transition occurred at 4.5 kbars, as expected.

The pressure vs temperature diagram for MnAs constructed on the basis of the experimental data is shown in Fig. III-2. The equation of the curve drawn through the data points above 200°K is $P = -5.623 + 1.073 T - (2.83 \times 10^{-4})T^2$, where P is the transition pressure in kbars, and T is the temperature in °K.

* Department of Metallurgy, M.I.T.

Section III

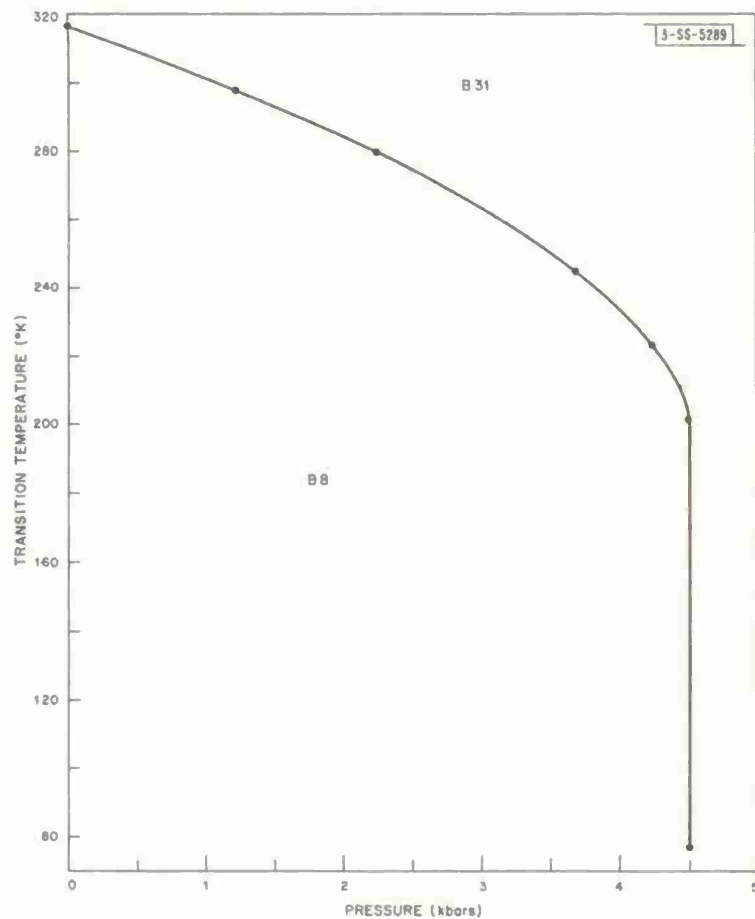


Fig. III-2. Pressure dependence of B8 \rightleftharpoons B31 transition temperature in MnAs.

The phase transformation was marked by an increasing degree of hysteresis as the temperature was decreased. At 77°K, in fact, the B31 phase did not transform back to the B8 phase even when the pressure was reduced to one atmosphere.

J. A. Kafalas
J. B. Goodenough

C. NEGATIVE MAGNETORESISTANCE IN Ti_2O_3

Negative magnetoresistance has been observed at 4.2° and, to a much smaller degree, at 77°K in single crystals of Ti_2O_3 doped with 1 to 3 atomic-percent V. Typical data for a crystal at 4.2°K, taken at the National Magnet Laboratory, are shown in Fig. III-3. The resistivity of this crystal is reduced from the zero-field value by about 10 percent at 170 kG, whereas in undoped single crystals, the resistivity increases by as much as 65 percent for the same temperature and field.¹⁰ The magnitude of the negative magnetoresistance for the V-doped crystals is independent of sample orientation but, as shown in Fig. III-3, depends slightly on the magnetic field orientation. The magnitude diminishes with increasing carbon and nitrogen impurity content. The results are the same for samples heated in vacuum to 400°C and then cooled in a field of 110 kG as for untreated samples.

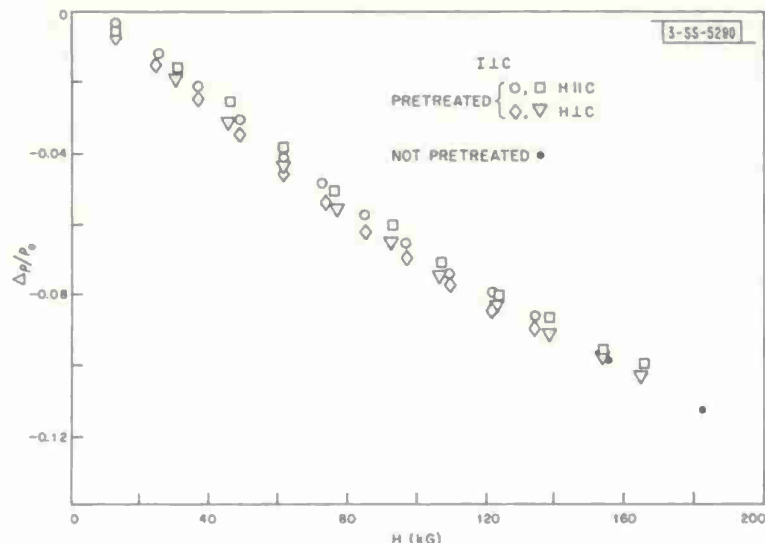


Fig. III-3. Negative magnetoresistance at 4.2°K of Ti_2O_3 containing 1.5 atomic-percent V.

In contrast with the negative magnetoresistance data reported for Ge (Ref. 11) and InSb (Ref. 12), the curves of $\Delta\rho/\rho_0$ for Ti_2O_3 do not exhibit saturation and do not change to a positive slope with increasing magnetic field. It is believed that the standard analysis¹³ is applicable to the present case of negative magnetoresistance, which is attributed to the presence of V with localized magnetic moments in the Ti_2O_3 lattice. The effect can be observed up to unprecedentedly high temperatures, apparently because competing positive magnetoresistance is minimized by the absence of broad bands in Ti_2O_3 .

J. M. Honig D. M. Esterling
L. L. Van Zandt R. E. Fahey

D. FIRST-ORDER LOCALIZED-ELECTRON \rightleftharpoons COLLECTIVE-ELECTRON TRANSITION IN $LaCoO_3$

Precision x-ray diffraction measurements of the atom positions in $LaCoO_3$ have been made at every 50°C from room temperature to 1000°C. The temperature dependence of the lattice parameters is shown in Fig. III-4. The crystal space group is $R\bar{3}c$ below 375°C and $R\bar{3}$ above 375°C. In the $R\bar{3}$ symmetry, there are two distinguishable octahedral cobalt positions, Co_I having larger crystalline fields than Co_{II} . Since high-spin and low-spin cobalt ions are simultaneously present, preferential long-range ordering of low-spin cobalt at Co_I sites and high-spin cobalt at Co_{II} sites occurs for $T < 375^\circ C$. Calorimetric data show a first-order transition at $T_t = 937^\circ C$ and a higher-order transition in the temperature interval $125^\circ < T < 375^\circ C$, which is also manifested in a large Debye-Waller factor in this interval and in a plateau in the curve of reciprocal susceptibility vs temperature. There is some evidence from DTA data of another higher-order transition at about 650°C. The electrical conductivity increases with increasing temperature below 650°C, but much more rapidly in the interval $125^\circ < T < 650^\circ C$ than below 125°C. It is nearly temperature-independent in the interval $650^\circ < T < 937^\circ C$ and is continuous through the first-order transition. However, above 937°C, the resistivity increases with temperature as in a metal. The space group remains $R\bar{3}$ and the pseudocubic cell edge is continuous

Section III

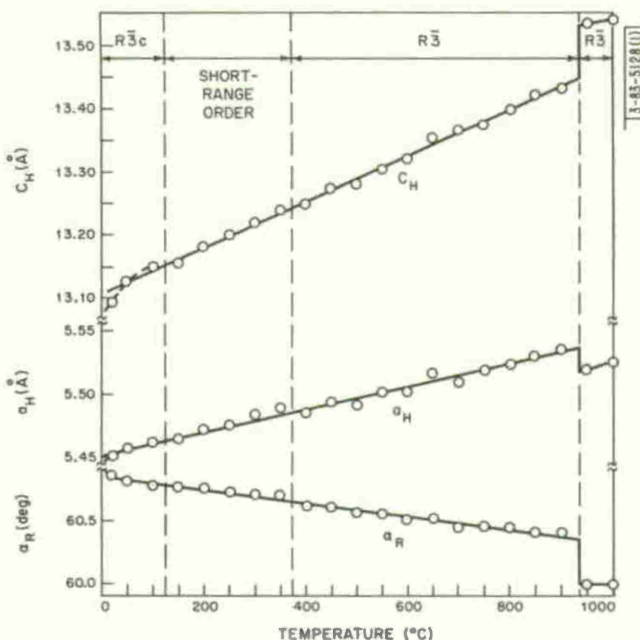


Fig. III-4. Temperature dependence of the lattice parameters of LaCoO_3 .

through the first-order phase change, but the rhombohedral angle drops abruptly from 60.40° to 60° and the La^{3+} ions are shifted discontinuously along the c -axis toward a Co_{I} ion. Similar La^{3+} -ion displacements occur in the temperature interval $400^\circ < T < 650^\circ\text{C}$. The Debye-Waller factor decreases by an order of magnitude on transformation to the high-temperature phase.

The data described are interpreted to indicate that (1) the first-order phase change at $T_t = 937^\circ\text{C}$ is a localized-electron \rightleftharpoons collective-electron transition for electrons in orbitals of e_g symmetry, higher temperatures introducing a Fermi surface and partial disproportionation between high-spin and low-spin cations at Co_{II} and Co_{I} positions, (2) the number of charge carriers is constant through the transition, because the number of localized charge carriers is saturated below T_t , and just above T_t , the bandwidth of the collective-electron states is less than kT , (3) the mobilities of the charge carriers are continuous through the transition, the activation energy for a localized-electron hop becoming much less than kT at $T < 937^\circ\text{C}$, (4) in the interval $125^\circ < T < 375^\circ\text{C}$, where the populations of high-spin and low-spin cobalt ions approach one another, there is a higher-order transition from a region of short-range order to an ordered phase occurring above 375°C , and (5) exciton transfer is an important mechanism in LaCoO_3 .

P. M. Raccah
J. B. Goodenough

E. TRAP-MEDIATED CATION-CATION BOND IN PbRuO_3 STRUCTURE

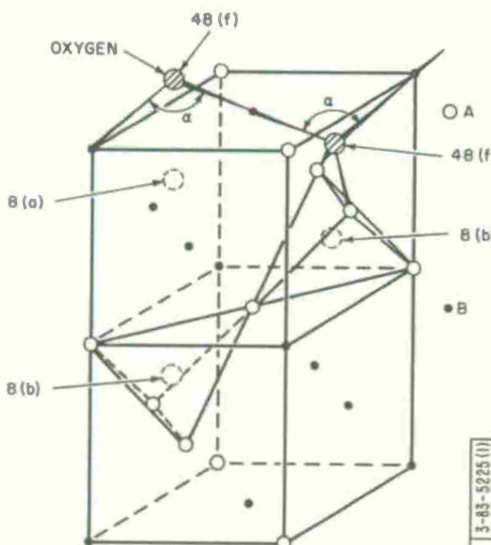
The compounds PbRuO_3 , PbIrO_3 , BiRhO_3 , and PbReO_3 have been synthesized for the first time. The first three compounds were prepared by reacting PbO with Ru metal, PbO with IrO_2 , and Bi_2O_3 with Rh metal, respectively, in air at 800°C . PbReO_3 was obtained by reaction of PbO and ReO_2 in an evacuated and sealed silica capsule at 750°C .

All four compounds are homogeneous black powders which have x-ray diffraction patterns of the face-centered-cubic pyrochlore type. The lattice parameters are: PbRuO_3 , 10.25 Å; PbIrO_3 , 10.27 Å; PbReO_3 , 10.42 Å; BiRhO_3 , 10.24 Å. The oxygen content for the Pb compounds was established by thermogravimetric analysis using H_2/Ar gas mixtures.

Lead ruthenate, PbRuO_3 , which was selected for more detailed study, was found to exhibit metallic conductivity. The resistivity of a pressed and sintered polycrystalline cylinder decreased from 2.7×10^{-4} ohm-cm at room temperature to 0.9×10^{-4} ohm-cm at 77°K. Consistent with metallic conductivity, the material is Pauli paramagnetic. The magnetic susceptibility is 25.98×10^{-6} emu/g, independent of temperature, between room temperature and 30°K. There is only a slight increase in susceptibility when the temperature is decreased from 30°K to liquid helium temperatures.

The pyrochlore structure for oxides with the formula $A_2B_2\text{O}_7$ has the space group $\text{Fd}3m$. The unit cell, which contains eight molecules, has large A cations in position 16(d), smaller B cations in position 16(c), and oxygen ions in positions 48(f) and 8(b), as shown in Fig. III-5. Since the composition of lead ruthenate corresponds to $\text{Pb}_2\text{Ru}_2\text{O}_6$ rather than $\text{Pb}_2\text{Ru}_2\text{O}_7$, there must be one oxygen vacancy per pyrochlore molecule. It is proposed that the oxygen vacancies are ordered at the 8(b) sites (also one per molecule) and that the structure is stabilized by trap-mediated cation-cation bonds between the four Pb ions which are arranged tetrahedrally around each oxygen vacancy. According to this model, the oxygen vacancy – like anion vacancies in the alkali halides – introduces a potential well for electrons at the 8(b) site. A subarray band containing three orbitals (six electron states) per molecule is formed by two orbitals of this potential well and one $6p_{\sigma}$ orbital supplied by the tetrahedral Pb ions. The potential well is deep enough to produce bonding between the four Pb ions by trapping one outer electron from each of the ions at the vacancy site. If the well is not deep enough to produce an appreciable energy gap between the four filled and two empty states of the subarray band, the band electrons will exhibit metallic conductivity.

Fig. III-5. Cation sublattice for one-quarter unit cell of pyrochlore structure.



Section III

In order to test the proposed model, integrated x-ray intensity measurements were made on PbRuO_3 powder with a Norelco diffractometer. Peaks which appeared to overlap were grouped in a single count. The data were then analyzed by a Fortran structure refinement program which adjusts the values of selected parameters in order to minimize the discrepancy between the observed and calculated line intensities. When the number of anion vacancies and their distribution over the 48(f) and 8(b) sites were taken as the parameters to be optimized, the program yielded a structure in which O^{2-} ions occupy all the 48(f) sites, as assumed by the proposed model, and also 42 percent of the 8(b) sites. This structure is apparently inconsistent with the composition of PbRuO_3 , since it corresponds to 6.4 rather than 6 O^{2-} ions per molecule. It can be reconciled with the composition, however, if the result for the 8(b) sites is interpreted in terms of electron density rather than O^{2-} concentration. Such an interpretation gives strong quantitative support to the proposed model, since 40 percent of the electron density of an O^{2-} ion corresponds to four electrons, just the number which the model assumes are transferred from the Pb ions and trapped at the 8(b) site.

Additional evidence for the trap-mediated bond model is obtained by considering the ionic radii of Pb in pyrochlore-type compounds, which can be estimated by comparing the unit cell edges for these materials with the cell edges of rare-earth pyrochlores. For compounds with typical pyrochlore structure, not containing anion vacancies, the estimated Pb radius is approximately the same as for Pb^{+2} . For PbRuO_3 , PbIrO_3 , and PbReO_3 , however, the estimated ionic radius is considerably reduced, and approaches the value for Pb^{+4} . This reduction can be explained by the transfer of two outer electrons from each Pb^{+2} ion to the 8(b) anion vacancy sites, as proposed by the trap-mediated model.

J. M. Longo
P. M. Raccah
J. B. Goodenough

F. $\text{YVO}_4:\text{Nd}$ LASER

Stimulated emission from Nd^{+3} in yttrium vanadate (YVO_4) was previously obtained¹⁴ at a pulsed threshold of about 200 J from a crystal grown by the Linde Corporation. Laser action has now been observed in substantially improved $\text{YVO}_4:\text{Nd}$ crystals from Linde at pulsed thresholds of only 2 to 3 J, which are comparable to those obtained for YAG:Nd lasers.

Yttrium vanadate crystallizes in the zircon (ZrSrO_4) structure. Its space group is D_{4h}^{19} . All rare-earth vanadates also have this structure and form solid solutions with YVO_4 in which the rare-earth ions substitute for Y^{+3} . Since the rare-earth ions in these solid solutions are situated in a strong tetragonal crystal field which lacks inversion symmetry, the probability of the parity-forbidden f-f transitions is increased. In comparison to YAG:Nd, therefore, the $^4\text{F}_{3/4}$ metastable level of Nd^{+3} in YVO_4 has an oscillator strength larger by a factor of six, a radiative lifetime (33 μsec) smaller by a factor of six, and an absorption coefficient larger by a factor of three.

Yttrium vanadate has strong absorption bands at wavelengths below 4000 Å because of Y-O and V-O charge transfer and $(\text{VO}_4)^{-3}$ molecular transitions. Strong yellow fluorescence is excited in the pure compound by 2537 or 3660 Å mercury radiation. This fluorescence is completely quenched in $\text{YVO}_4:\text{Nd}$ crystals. The quenching is attributed to energy transfer from the host lattice to the Nd^{+3} ions.

J. R. O'Connor

G. WET CHEMICAL ANALYSIS OF PbTe-SnTe ALLOYS

An analytical method based on automatic potentiometric EDTA titrations has been developed for the determination of lead and tin in PbTe-SnTe alloys. Samples are dissolved in a mixture of 3:1 HNO₃-HCl. The sum of lead and tin is determined at pH 4.5 by adding a known excess of standardized EDTA and back-titrating with standard lead solution. Lead is determined by a back titration with lead on a separate sample aliquot at pH 6.2 after using tartaric acid to mask tin. Tin is determined by difference. A mercury cup electrode and a saturated calomel electrode are used as the indicator and reference electrodes, respectively, for both titrations. In analyses of synthetic standards, accuracies of one to two parts per thousand have been obtained for titrant volumes in the two- to ten-milliliter range.

J. C. Cornwell

REFERENCES

1. Solid State Research Report, Lincoln Laboratory, M.I.T. (1966:2).
2. B.W. Howlett, J.S. Li. Leach, L.B. Ticknor and M.B. Bever, Rev. Sci. Instr. 33, 619 (1962).
3. The calorimetric measurements were carried out at the M.I.T. Materials Science Center under the sponsorship of the Office of Naval Research, Contract Nonr-3963-(19).
4. P.M. Robinson and M.B. Bever (to be published).
5. J.S. Kasper and H. Brandhorst, J. Chem. Phys. 41, 3768 (1964).
6. D.B. McWhan and M. Marezio (to be published).
7. J.E. Martin and P.L. Smith, Brit. J. Appl. Phys. 16, 495 (1965).
8. Solid State Research Report, Lincoln Laboratory, M.I.T. (1965:3), p. 31, DDC 629048.
9. Solid State Research Report, Lincoln Laboratory, M.I.T. (1965:1), p. 50, DDC 622446, H-678.
10. Solid State Research Report, Lincoln Laboratory, M.I.T. (1966:1), p. 25, DDC 632998, H-721.
11. W. Sasaki and R.B. Ouboter, Physica 27, 877 (1961).
12. R.P. Khosla and R.J. Sladek, Proceedings of the International Conference on the Physics of Semiconductors, Kyoto, 1966 (to be published).
13. Y. Toyozawa, J. Phys. Soc. Japan 17, 986 (1962).
14. Ref. 10, p. 28.

IV. PHYSICS OF SOLIDS

A. ELECTRONIC BAND STRUCTURE

1. Electroreflectance in Metallic Oxides

We have employed the sensitive electroreflectance modulation technique¹⁻³ in an effort to learn more about the band structure of the conducting oxides, ReO_3 and the sodium tungsten bronzes, from optical measurements. In one form of this method, the reflectivity R of the material is modulated by the high longitudinal electric field occurring at the interface between the sample and an electrolyte when a small bias voltage is applied.² An AC modulating voltage is imposed on the bias voltage, and phase sensitive detection is used to obtain a sensitivity in $\Delta R/R$ of the order of 10^{-5} .

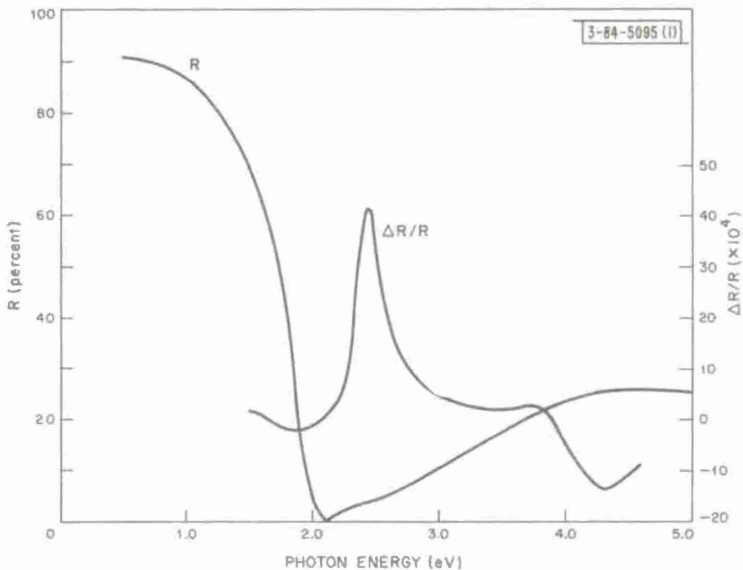


Fig. IV-1. Comparison between $\Delta R/R$ and R for a tungsten bronze sample.

Preliminary work by this technique has shown that large signals are obtained in sodium tungsten bronze samples of high conductivity, and the structure observed in $\Delta R/R$ corresponds closely to structure seen in ordinary reflectivity. The spectrum of $\Delta R/R$ is shown in Fig. IV-1 for one sample of sodium tungsten bronze along with the spectrum of absolute reflectivity of this sample. The free electron plasma edge occurs near 2.0 eV where a negative minimum appears in the electroreflectance. A sharp positive peak in $\Delta R/R$ occurs near 2.3 eV, which may be the onset of interband transitions.⁴ From the reflectivity data, other interband transitions are believed to occur near 4.0 eV, and these appear as a negative peak in the electroreflectance. These data, although preliminary in nature, demonstrate that this technique may be useful for determining interband transition energies. A comparison of the interband structure among similar oxides will aid in resolving band structure.

J. Feinleib B. Feldman
W. J. Scouler

Section IV

2. Modulated Reflectance of Germanium in the Ultraviolet

A recent paper⁵ has reported another method of modulating the reflectance of a semiconductor in which a pulsed electric current is passed through the sample. The reflected light signal which is synchronous with the pulse frequency is then detected using a lock-in amplifier. Small changes in the reflectivity due to the modulating field can then be observed. This method has the advantage over the electrolytic electroreflectance technique in avoiding the use of an electrolyte which is desirable when (a) the sample reacts with the electrolytes, (b) the electrolyte limits the range of measurement, which is the case in the ultraviolet region where we operate, or (c) low-temperature measurements are required.

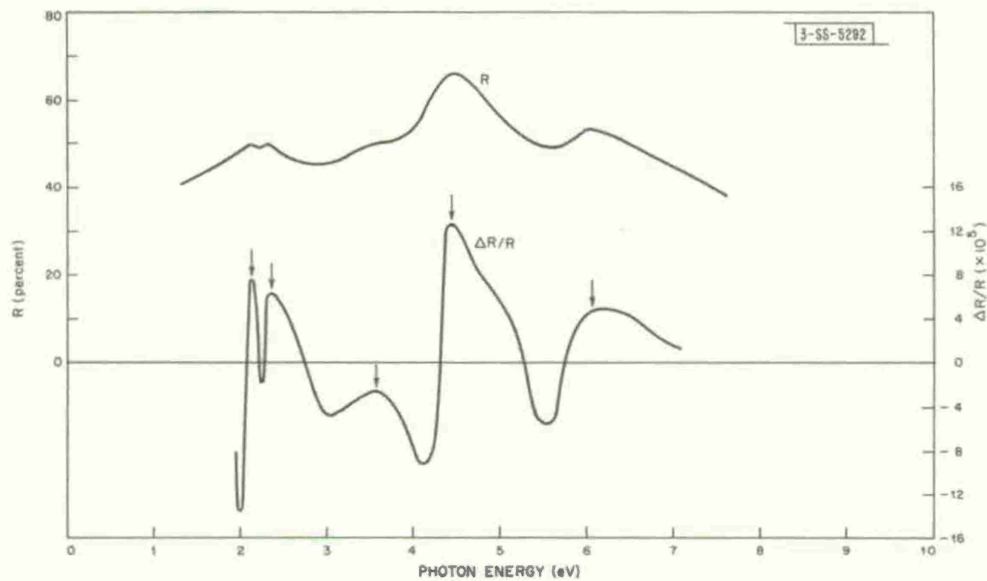


Fig. IV-2. Comparison between $\Delta R/R$ and R for germanium.

Figure IV-2 shows $\Delta R/R$ and R for a 0.005-inch-thick, polished and etched germanium sample at about 77°K. The pulse frequency was 12 Hz, the pulse width about 5 msec, and the peak voltage about 100 V. A tungsten lamp was used as a light source below 3.5 eV, and a hydrogen gas discharge was used above 3.5 eV. The photomultiplier output was fed into a lock-in amplifier. The curve is similar to that recently reported for germanium by the electrolyte method.⁶ However, not as much fine structure appears here. The arrows point to peaks or shoulders observed in normal reflectance measurements.

The peak widths, heights, and positions are sensitive to pulse voltage, width, and frequency. The following observations made while varying these parameters suggest that the modulation effect is due to pulsed $I^2 R$ heating of the sample: (a) The signal deteriorates at higher frequencies; if the effect were thermal, then one would expect that the finite heat capacity of the sample would not permit a fast response. (b) Increasing the power input pushes the peaks toward lower energies; a heating effect would give this result also. However, the signal seems strongest when maximum power is put into the sample, although there is a limit since the sample undergoes some kind of avalanche breakdown during long and/or high voltage pulses.

Since the method appears promising, it is hoped that it can be extended to materials that do not readily lend themselves to the electrolyte technique.

W. J. Scouler

3. Electroreflectance in Metals

The electroreflectance technique has been useful for semiconductor investigations because the electric field can penetrate the material to a sufficient depth, the order of the wavelength of light, so that the light can interact with the modulated band structure. In metals, it was predicted that the electric field penetration of only $\sim 1 \text{ \AA}$ is too small to have an effect on the optical constants and thus no electroreflectance modulation should be observed. We have shown that this prediction does not hold⁷ and that samples of the noble metals (silver, copper, and gold) have given large electroreflectance signals corresponding to known structure in the reflectivity of the metals. This method is being used to study the noble metals and the ferromagnetic metals. We are also trying to study the phenomenon itself.

J. Feinleib
G. F. Dresselhaus
B. Feldman

4. Infrared Magneto-Electroreflectance in Germanium, GaSb, and InSb[†]

The electroreflectance technique,¹ using an electrolyte,² has been useful for studying the Group IV and III-V semiconductors in the range from 1 to 6 eV. We have succeeded in extending the range to the near infrared, $\sim 0.5 \text{ eV}$, and this has permitted the study of magneto-optical effects near the direct gap and at the split-off valence band to conduction band transition in germanium and InSb by this technique. The results of these studies are shown in Figs. IV-3, IV-4, and IV-5. From these data, we obtain a direct gap at $k = 0$ for germanium at room temperature to be 0.801 eV, and for p-type GaSb to be 0.74 eV. The split-off valence band to conduction band gap at $k = 0$ is found at 1.083 eV in germanium and at 0.79 eV in InSb. From the observed Landau level structure at fields up to 100 kG, the conduction band mass in germanium was calculated to be $(0.042 \pm 0.005) \text{ m}$, and the split-off valence band mass to be $(0.084 \pm 0.01) \text{ m}$. These values for germanium are in good agreement with the values obtained from magneto-piezoreflection data by Mavroides, Dresselhaus, Aggarwal and Dresselhaus⁸ and with the theoretical estimates of Dresselhaus, Kip and Kittel.⁹ This work has been submitted for publication.

S. H. Groves
C. Pidgeon[‡]
J. Feinleib

5. Magneto-Piezo-Optical Studies in Semiconductors[§]

Preliminary room-temperature results of magneto-piezoreflection experiments in germanium and InSb have demonstrated that acoustical modulation of the magnetoreflection enhances the

[†]Part of this work was carried out using the high field facilities of the National Magnet Laboratory, M.I.T.

[‡]National Magnet Laboratory, M.I.T.

[§]This work was carried out using the high field facilities of the National Magnet Laboratory, M.I.T.

Section IV

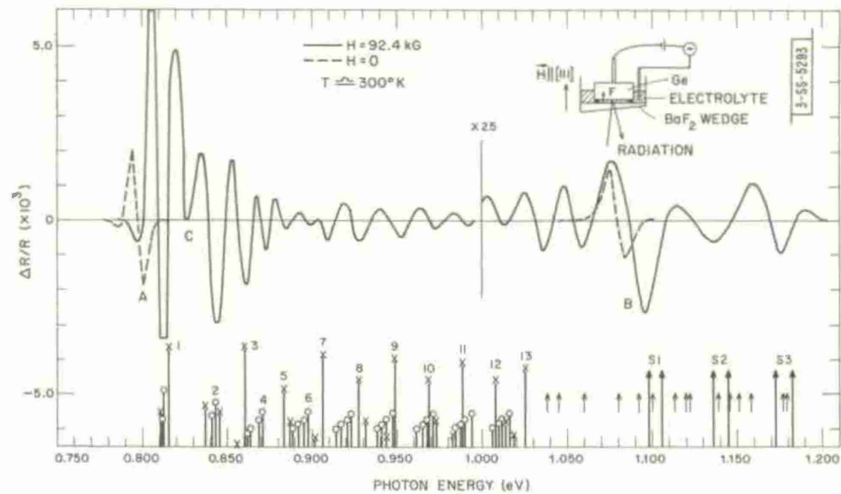


Fig. IV-3. Interband electroreflectance in germanium for $H = 0$ and 92.4 kG in the parallel electric and magnetic field configuration. Theoretical energies and relative strengths are shown for allowed light hole x and heavy hole o to conduction band transitions up to 1.03 eV. Above this energy, positions of principal valence to conduction band transitions are indicated by small arrows. Relative strengths and positions of all allowed split-off band to conduction band transitions are shown by large arrows. Inset shows the experimental arrangement.

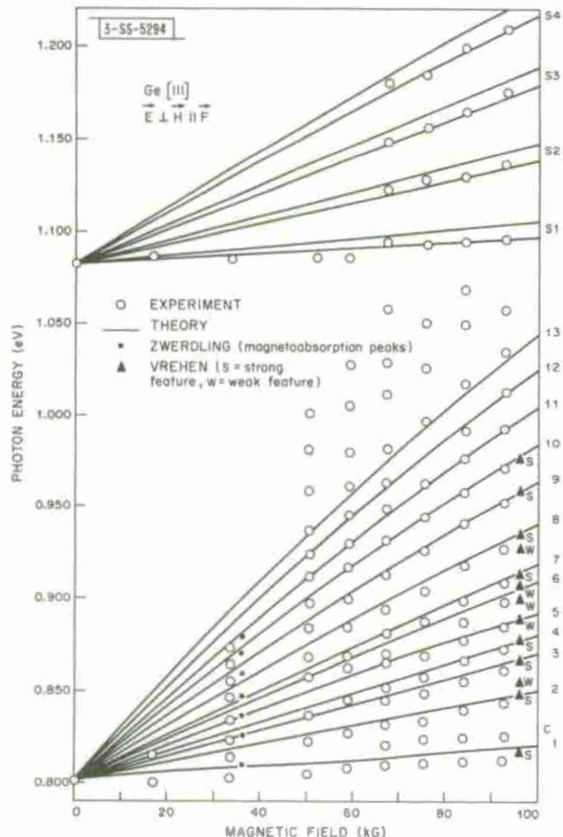


Fig. IV-4. Plot of photon energy of magneto-electroreflectance minima as a function of magnetic field. The principal allowed valence to conduction band transitions are labeled 1 to 13; split-off band to conduction band transitions are labeled S1 to S4.

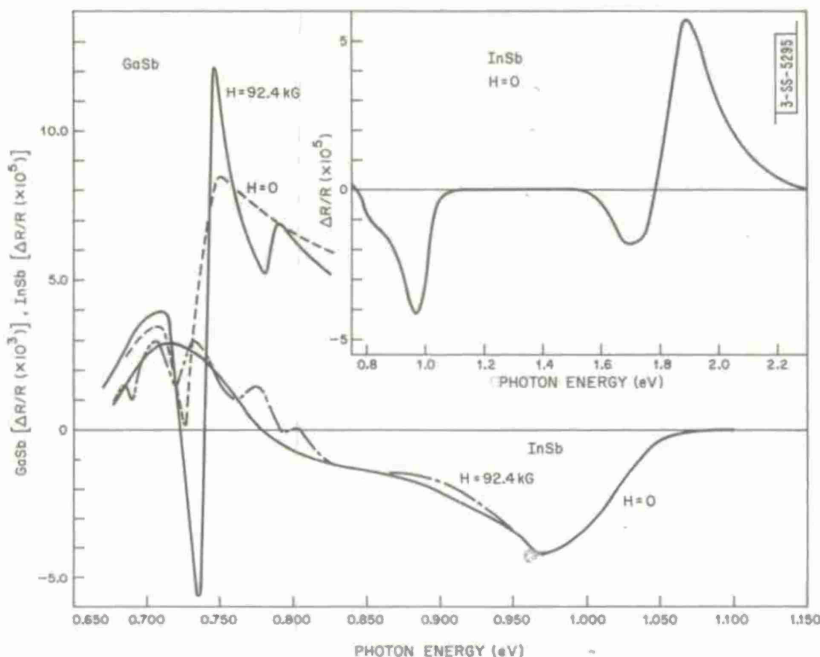


Fig. IV-5. Electroreflectance in region of absorption edge in GaSb and of split-off band to conduction transitions in InSb for $H = 0$ and 92.4 kG. Inset shows relative magnitude of electroreflectance associated with split-off band transition at $k = 0$ and with λ -point transition in InSb.

optical structures which are identified with interband transitions. In connection with the room-temperature results on the direct gap in germanium which were reported previously,¹⁰ an attempt was made to obtain an experimental criterion for locating the resonance position within the zero-field piezoreflection linewidth by studying the magnetic field dependence of the piezoreflection maxima, minima, and inflection points corresponding to the lowest interband transition. As shown in Fig. IV-6, these three positions on the magnetic field resonance line extrapolate to the inflection point of the zero-field piezoreflection line, which suggests that the energy gap is determined from the photon energy corresponding to this point.

A criterion for the determination of the resonance point within the magneto-piezoreflection linewidth was established by comparing the magnetic field and photon energy dependences of the piezoreflection maxima, minima, and inflection points with the room-temperature magnetoabsorption data.¹¹ The best fit was obtained by taking the resonance point at the magneto-piezoreflection maxima.

A summary of the interband transitions observed on a (111) face of germanium is given in Fig. IV-7. Here we have plotted the position in photon energy and magnetic field of the piezoreflection maxima. The value for the direct bandgap obtained from these data is 0.795 eV, which is somewhat lower than the value of 0.803 eV obtained from magnetoabsorption. Using a value of $m_v = 0.375 m^8$ for the valence band, $m_c = 0.041 m$ was found for the conduction band, which compares well with the magnetoabsorption data of Zwerdling¹¹ and also with the recent magneto-electroreflectance work.¹²

Section IV

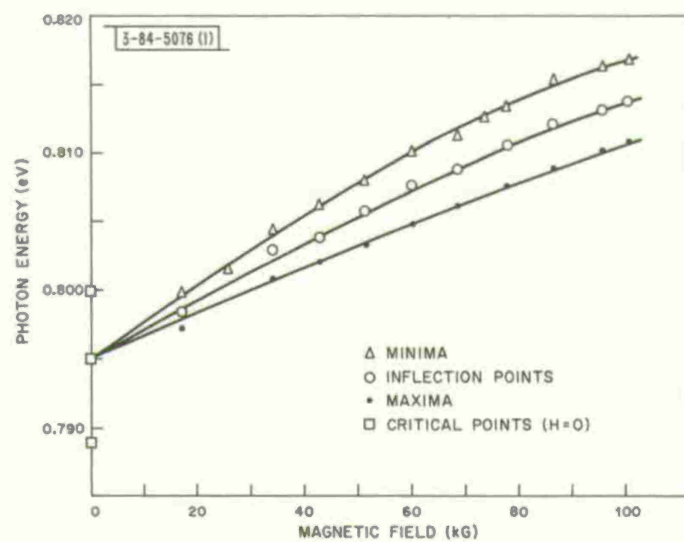


Fig. IV-6. Magnetic field dependence of piezoreflection critical points.

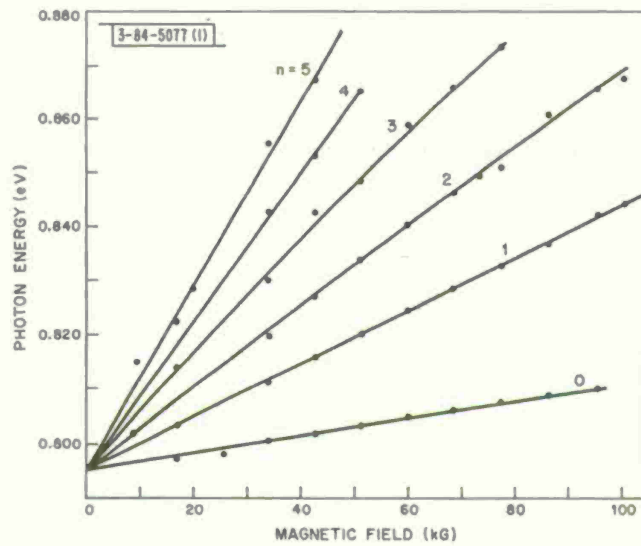


Fig. IV-7. Interband transitions across direct bandgap of germanium.

Among the new effects studied in germanium have been the magnetic field dependence of the interband transitions across the indirect bandgap involving the absorption of a phonon, and the direct Landau level transitions from the spin-orbit split-off band to the conduction band at $\vec{k} = 0$. A recorder trace showing the latter transitions is given in Fig. IV-8 for $H \perp$ (100) face. Arrows pointing downward indicate the location of the resonances expected at 1.13 eV using $m^*/m = 0.041$ and 0.074 for the conduction and split-off valence bands, respectively. The arrows pointing upward give the corresponding resonance locations for transitions across the lowest direct bandgap. For the $n = 1$ transition, the experimental trace exhibits a splitting. Analysis of traces like that of Fig. IV-8 yields a value for the spin-orbit split-off bandgap of 1.08 eV, which may be compared with the value of 1.09 eV, obtained from electroreflectance studies,¹ and of 1.083 eV,¹² obtained from magneto-electroreflectance.¹²

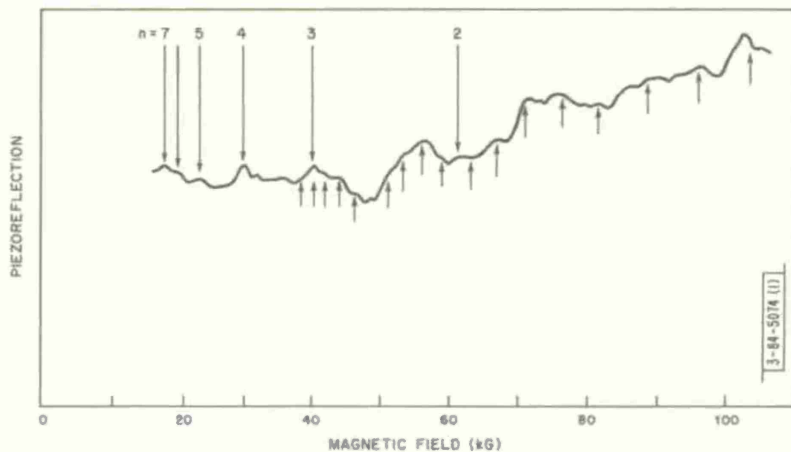


Fig. IV-8. Magneto-piezoreflection in germanium at 1.13 eV.

With the magneto-piezoreflection technique, an impressive enhancement is also found for the resonances identified with interband transitions across the direct gap in InSb, as seen in Fig. IV-9, where a comparison is made between the magnetoreflection and magneto-piezoreflection at 0.253 eV for a (100) face. The fan chart constructed from such traces exhibits the nonparabolic behavior associated with the small effective mass and bandgap in InSb; fairly good agreement is obtained with the corresponding curves obtained from magnetoabsorption.¹³

J. G. Mavroides
Mildred S. Dresselhaus
G. F. Dresselhaus
D. F. Kolesar

6. Far Infrared Zeeman Effect of Group III Impurities in Germanium[†]

Experimentally, we have demonstrated that under large magnetic fields, the Zeeman effect splits the C and D lines of the excitation spectra of the Group III impurity, gallium, in germanium into three and eight components, respectively.¹⁴ This is in contrast to the work of others¹⁵ in which only two lines were resolved for each of the C and D lines.

[†]This work was carried out using the high field facilities of the National Magnet Laboratory, M.I.T.

Section IV

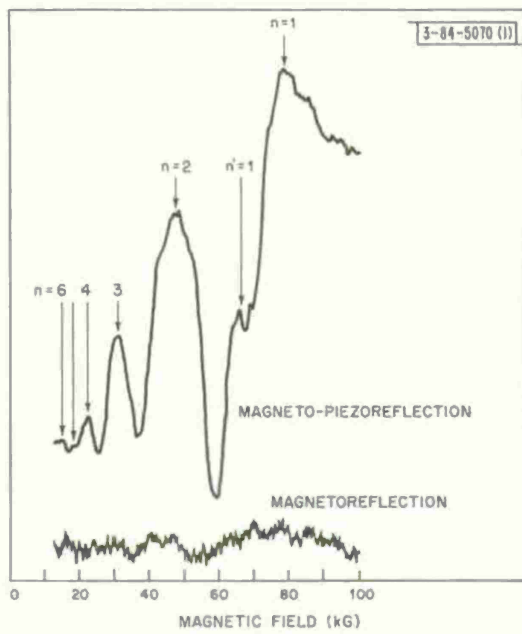


Fig. IV-9. Recorder traces from (100) face of InSb.

We are now attempting to make measurements as a function of temperature in order to observe the effect of varying the relative population of the ground state levels.

These results of the Zeeman effect and the results of the effect of stress¹⁴ on the same impurity system should give a complete description of the levels involved in the excitation spectra of the Group III impurities in germanium.

D. H. Dickey
M. J. Fulton

7. Electron-Phonon Interaction in n-InSb at 9 GHz

The propagation of 9-GHz longitudinal ultrasonic waves has been studied in n-InSb at temperatures between 4.2° and 36°K and in magnetic fields up to 25 kG for several crystal orientations and electron concentrations, with particular emphasis on the electronic contribution to the attenuation and velocity of the ultrasonic wave. These experiments have yielded a direct determination of the magnitude of the piezoelectric constant e_{14} and the conduction band deformation potential C_1 for InSb. They also represent the first ultrasonic measurements in semiconductors in the range where the electron mean free path ℓ is greater than the wavelength of the sound. In our samples, $q\ell \sim 5$, where q is the ultrasonic wavevector.

The theoretical expressions for the change in attenuation $\Delta\alpha$ and the dispersion $\Delta v_s/v_s$ due to the magnetic field B can be written in terms of the total longitudinal dielectric constant $\epsilon_\ell = \kappa\epsilon_0 - \sigma(\omega, q, B)/i\omega$, which includes the lattice dielectric constant $\kappa\epsilon_0$ and the electron polarizability $-\sigma/i\omega$:

$$\Delta\alpha = -K^2 q \operatorname{Im} \left[\frac{\kappa\epsilon_0}{\epsilon_\ell(B)} - \frac{\kappa\epsilon_0}{\epsilon_\ell(0)} \right] ; \quad \frac{\Delta v_s}{v_s} = \frac{K^2}{2} \operatorname{Re} \left[\frac{\kappa\epsilon_0}{\epsilon_\ell(B)} - \frac{\kappa\epsilon_0}{\epsilon_\ell(0)} \right]. \quad (1)$$

The coupling constant $K^2 = K_p^2 + K_d^2$, where K_p and K_d are proportional to e_{14} and C_1 , respectively. It has been necessary to extend previous calculations^{16,17} of ϵ_ℓ for the case of

nondegenerate statistics to include electron recoil, a quantum effect that has been quite negligible in previous experiments, but which here is so large that the electron-phonon interaction should be viewed as Bragg scattering rather than resonant Landau damping.¹⁸ Also in contrast to the usual Boltzmann equation treatment, the quantum calculation including recoil predicts that the attenuation for $B = 0$ is collision-independent only for $\omega\tau \gg 1$ instead of the more easily obtainable condition $q\ell \gg 1$. The assumption of a constant electron collision time τ which is made in the theory is adequate to explain the data in the low-field region (below about 5 kG) where C_1 and e_{14} were determined. However, the high-field behavior for propagation along and across the field has not been satisfactorily explained. The generalization to a velocity-dependent τ may be sufficient to account for the high-field observations, but this has not been attempted. Interpretation of the data for the samples at 4.2°K is also complicated by the magnetic field dependence of the electron concentration.

We now discuss the determination of C_1 and e_{14} from the magnetic field dependence of the attenuation for propagation across the field at 18°K. This method has allowed the determination of C_1 and e_{14} independently, since $\langle 111 \rangle$ longitudinal waves are piezoelectrically coupled to the electrons, whereas $\langle 100 \rangle$ and $\langle 110 \rangle$ longitudinal waves are coupled via the deformation potential only. The data were taken using a sensitive microwave receiver in an interferometer circuit¹⁹ which could measure a velocity change of about 1 part in 10^7 and a total insertion loss as high as 170 dB. Evaporated thin films of CdS were used as transducers.

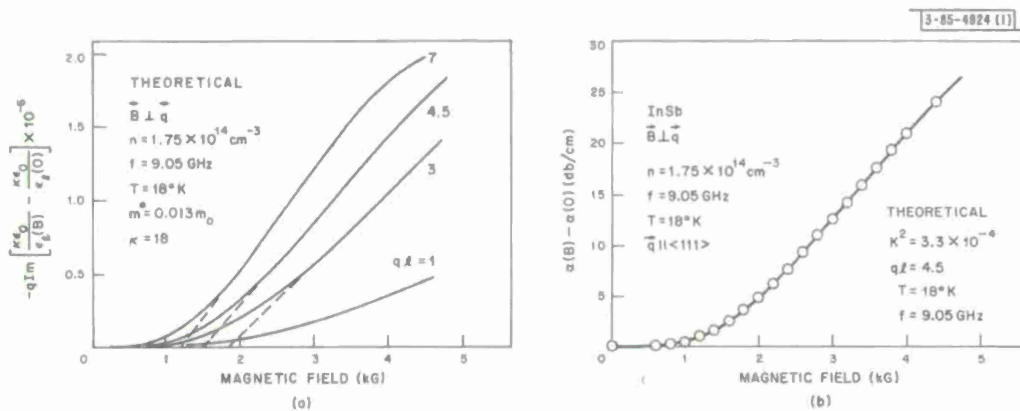


Fig. IV-10(a-b). Comparison of theory with experimental attenuation data on $\langle 111 \rangle$ sample.

Figure IV-10(a) gives the theoretical attenuation for several values of $q\ell$, normalized to the coupling constant K^2 . The shape, and, in particular, the low-field intercept, determines $q\ell$; K^2 is then determined by scaling. This procedure gives the result shown in Fig. IV-10(b) for data taken on a $\langle 111 \rangle$ sample. The magnitude of the piezoelectric constant is found from these data to be $|e_{14}| = 0.06 \text{ C/m}^2$. This value is also consistent with the velocity change to 4 kG. Similar data for a $\langle 100 \rangle$ sample are shown in Fig. IV-11 from which a value is obtained for the magnitude of the conduction band deformation potential of $|C_1| = 4.5 \text{ eV}$. The deformation potential coupling accounts for about 2 percent of the observed attenuation in the $\langle 111 \rangle$ sample.

Velocity and attenuation data for propagation along the magnetic field at 4.2° and 18°K are shown in Fig. IV-12. A smooth curve is drawn through the data points. The initial decrease in

Section IV

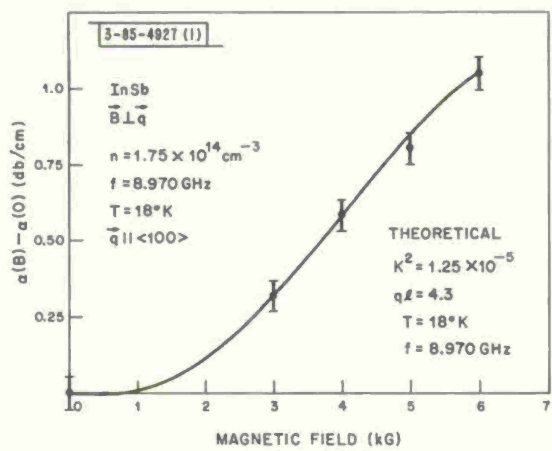


Fig. IV-11. Comparison of theory with experimental attenuation data on $\langle 100 \rangle$ sample.

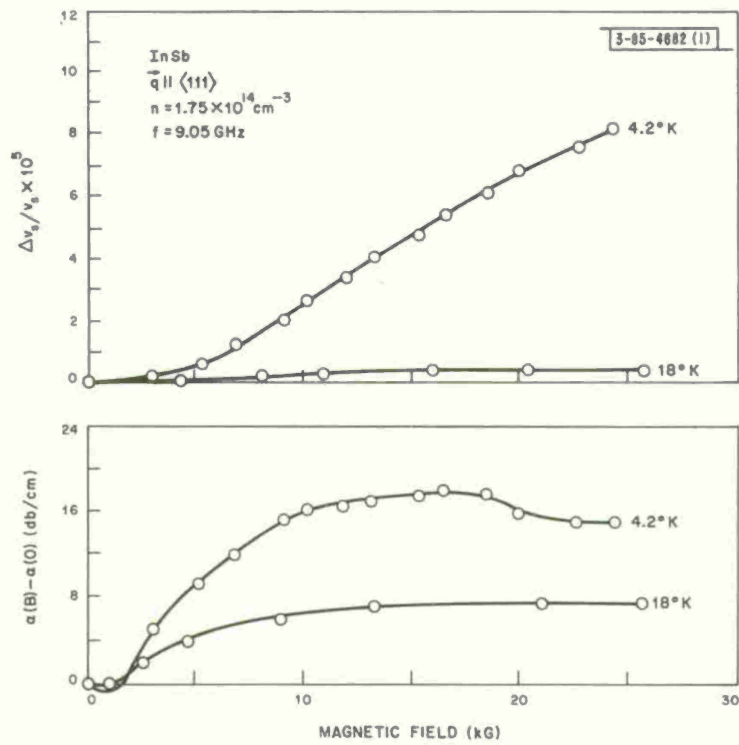


Fig. IV-12. Velocity and attenuation data on $\langle 111 \rangle$ sample for propagation along magnetic field.

attenuation observed at 4.2°K for magnetic fields below 1 kG is also present in the data taken for propagation across the field at 4.2°K. This anomalous behavior occurs at the same fields as an observed negative magnetoresistance^{20,21} at 4.2°K, which has been ascribed to scattering by electrons localized in magnetic states around donor impurities.

K. W. Nill
A. L. McWhorter

8. Effect of Electron-Longitudinal Optical Phonon Interaction on Energy of Bound Exciton States in a Magnetic Field

Recent interband magnetoabsorption experiments²² in InSb have shown strong nonlinearities in the absorption energy as a function of magnetic field. These have been interpreted as being effects of the electron-LO phonon interaction on the conduction band Landau levels.

However, according to Elliot and Loudon²³ (henceforth, EL), the states excited in high-field interband magnetoabsorption are almost entirely bound excitons with center-of-mass kinetic momentum, Π_{cm} , nearly equal to zero. It is therefore of interest to study the effect of the electron-LO phonon interaction on the energy of bound exciton states in strong magnetic fields.

The effective mass Hamiltonian in a simple parabolic band for the electron-hole pair can be written:

$$\mathcal{H} = \mathcal{H}_0 + V(|r_e - r_h|) \quad (2)$$

$$\mathcal{H}_0 = \frac{(p_e + \frac{e}{2c} H \times r_e)^2}{2m_e} + \frac{(p_h - \frac{e}{2c} H \times r_h)^2}{2m_h} \quad (3)$$

where the subscripts e and h refer to electron and hole, respectively. We observe that if we take

$$\Pi_{cm} = p_e + p_h + \frac{e}{2c} H \times (r_e - r_h) \quad (4)$$

then

$$[\Pi_{cm}, \mathcal{H}] = 0 \quad (5)$$

so that Π_{cm} is a constant of the motion.

The eigenfunctions of Eq.(3) can be chosen to be simultaneous eigenfunctions of \mathcal{H}_0 and Π_{cm} , where Π_{cm} is the component of Π_{cm} perpendicular to H . Rewriting Eq.(3) in relative coordinates, EL have found the subset of eigenfunctions of \mathcal{H}_0 corresponding to $\Pi_{cm} = 0$. Since the electron-phonon interaction couples states with $\Pi_{cm} = 0$ to states with $\Pi_{cm} \neq 0$, it is necessary to complete the solution of Eq.(3). We have done this and have obtained eigenfunctions

$$\begin{aligned} \psi_{\Pi, N, L} \propto & \exp \left[\frac{i}{\hbar} \left(\frac{m_h - m_e}{2M} \right) \Pi_{cm} \cdot \underline{z} \right] \exp [i |L| \varphi] \sigma^{|L|/2} \\ & \times \exp \left[-\frac{\sigma}{2} \right] \exp \left\{ \frac{i}{\hbar} [p_z(z_e - z_h) + \Pi_{cm} \cdot \underline{R}] \right\} \\ & L_N^{|\underline{L}|(\sigma)} \\ & L_{N+L}^{|\underline{L}|(\sigma)} \end{aligned} \quad (6)$$

Section IV

where $M = m_e + m_h$, $\sigma = (eH/2\hbar c) r^2$, $r = [x_e - x_h + (eH/c)^{-1} \Pi_{ycm}] u_x + [y_e - y_h - (eH/c)^{-1} \Pi_{xcm}] u_y$, with u_x and u_y unit vectors along x and y , respectively. We have assumed that $H = H u_z$. The upper function in the brackets of Eq. (6) is to be used for $L \geq 0$ and $R = (m_e r_e + m_h r_h)/M$. The eigenvalue associated with $\psi_{II, N, L}$ is

$$E = \frac{e\hbar H}{c} \left[\frac{1}{\mu} \left(N + \frac{1}{2} \right) - \frac{1}{m_h} L \right] + \frac{p_z^2}{2\mu} + \frac{\Pi_z^2}{2M} \quad (7)$$

where $1/\mu = (1/m_e) + (1/m_h)$, and $L \leq N$.

The degeneracy of $\psi_{II, N, L}$ with respect to Π_{\perp} , evident from Eq. (7), can be understood from the fact that Π_{\perp} is proportional to the separation of the center of the orbits of electron and hole.

In the presence of $V(|r_e - r_h|)$, the degeneracy in Π_{\perp} is lifted, and it is very reasonable to expect that for small Π_{\perp} , the dependence of the energy on Π_{\perp} is given by

$$\gamma f(\Pi_{\perp}^2) + \frac{\Pi_z^2}{2M} \quad \text{where} \quad f(\Pi_{\perp}^2) \rightarrow \begin{cases} \Pi_{\perp}^2 & \text{as } \Pi_{\perp}^2 \rightarrow 0 \\ 0 & \text{as } \Pi_{\perp}^2 \rightarrow \infty \end{cases} \quad (8)$$

and where the positive constant γ is a monotonic function of some average strength of $|V(r)|$.

Notwithstanding the spectrum given by Eq. (8), we would expect that for γ sufficiently small, the pinning of one bound exciton to another should be qualitatively similar to the pinning of one Landau level to another.

D. M. Larsen

9. Band Structure of TiO_2 in the LCAO Approximation

The 34×34 secular determinant for the TiO_2 (rutile) structure has been set up using the method of Slater and Koster.²⁴ The unit cell contains six inequivalent atoms – two titanium and four oxygen. We considered linear combinations of the 3d, 4s and 4p Löwdin functions on Ti and of the 2s and 2p Löwdin functions on O. The interactions considered were Ti to nearest equivalent Ti, Ti to nearest inequivalent Ti, and Ti to nearest O. The O-O interactions were all neglected (other than self-interactions).

It remains to factor the determinant using the point group of the crystal. In addition, further simplifications may be obtained by considering only the nearest-neighbor interactions, and also by investigating special cases along certain symmetry directions.

While working on the above structure, the possibility arose of programming the technique for an arbitrary crystal structure. This is currently being investigated.

D. M. Esterling
J. M. Honig

10. Band Structure Calculations on TiO , TiN , and TiC

In continuation of prior work,²⁵ we have determined the numerical values of the 24 transfer integrals that appear in the LCAO approximation scheme²⁴ for the band structures of TiO , TiN , and TiC . The quantities were determined from the eigenvalues corresponding to special symmetry

points in the Brillouin zone, on the basis of APW calculations. Initially, the 10×10 secular determinant, resulting from the use of Ti 3d, 4s and anion 2s, 2p functions as a basis, was reduced in size by specializing to the $\langle 100 \rangle$, $\langle 110 \rangle$, and $\langle 111 \rangle$ symmetry directions in the unit cell. The resulting subdeterminants were then expanded to yield 21 algebraic functions $F_i(\lambda)$ involving all the parameters. Insertion of the eigenvalues for each substance led to sets of systems of 36 equations in 24 parameters. On constructing a general function of the type $G = \sum_i F_i(\lambda_j) i = 1, \dots, 21, j = 1, \dots, 36$, and using algebraically obtained requisite partial derivatives $\partial G / \partial P_k$, where P_k is one of the 24 parameters, a computer program, employing Davidon's method,²⁶ was written to determine the parameters which minimize G . Machine time on the SDS 930 averaged five minutes for each case execution. The minimum G values were $G = 1.21 \times 10^{-3}$, 1.17×10^{-3} , and 0.622×10^{-3} , for TiO, TiN, and TiC, respectively.

Listings of the transfer integrals $\langle \psi_i | H | \psi_j \rangle$ are shown in Table IV-1. The first two symbols designate the wave functions. The Miller indices indicate the relative positions of the atoms under study in the unit cell.

Further refinements of these calculations are in progress.

W. C. Mason Virginia J. Mason	J. M. Honig J. O. Dimmock
----------------------------------	------------------------------

B. MAGNETISM

1. Low-Temperature Crystallographic and Magnetic Study of LaCoO₃

The structural and magnetic properties of LaCoO₃ have been studied between 300° and 4.2°K. Previous investigators have usually reported the existence of a local maximum in the susceptibility at 90°K in this material, but a recent single-crystal study by Naiman, *et al.*,²⁷ indicated no such phenomenon. We find that the magnetic properties in chemically pure materials are strongly dependent on the method of preparation. Thus we have been able to obtain samples exhibiting a susceptibility maximum, and then remove it by additional regrinding and refiring.

Samples with and without a susceptibility maximum were studied using neutron diffraction. Our results indicate that both sample types have $\bar{R}\bar{c}$ symmetry at room temperature and below. In addition, neither type exhibits any long-range bulk magnetic order at 4.2°K. This result is in accord with that of Koehler and Wollan.²⁸

Both sample types were studied with a vibrating-coil magnetometer. An anomalously rapid increase of magnetic moment with decreasing temperature was observed below 40°K in a field of 10 kOe. The presence of a small ferromagnetic component was established by the presence of hysteresis at 4.2°K, a trace of this hysteresis remaining at 77°K. The magnetic moment, as measured in 200 Oe, was found to decrease gradually with increasing temperature above 4.2°K. The absence of any abrupt drop indicates the remanent moment to be due to isolated magnetic regions in a nonmagnetic matrix. The apparent presence of a nonmagnetic matrix coupled with the absence of any long-range magnetic order leads us to conclude that the ground state of the cobalt ion in LaCoO₃ is diamagnetic Co^{III}.

N. Menyuk K. Dwight P. M. Raccah
--

Section IV

TABLE IV-1 NUMERICAL VALUES OF TRANSFER INTEGRALS DETERMINED FROM 10×10 SECULAR DETERMINANTS FOR TiO, TiN, AND TiC				
Self-Interactions				
Orbitals	Miller Indices	Energy (Ry)		
		TiO	TiN	TiC
$z^2 z^2$	000	0.873	0.838	0.887
$s_c s_c$	000	0.732	1.359	1.470
$XY XY$	000	0.636	0.702	0.694
$x_a x_a$	000	0.0989	0.469	0.637
$s_a s_a$	000	-0.942	-0.356	-0.00958
Nearest-Neighbor Interactions				
$z^2 z_a$	001	± 0.116	± 0.117	± 0.124
$s_c s_a$	100	± 0.0937	± 0.0583	± 0.0204
$s_c x_a$	100	± 0.0777	± 0.00714	± 0.0291
$XY x_a$	010	± 0.0622	± 0.0650	± 0.0714
$z^2 s_a$	001	0.0595	-0.0737	0.0822
Next-Nearest-Neighbor Interactions				
$XY XY$	110	-0.0528	-0.0302	-0.0286
$x^2 - y^2 x^2 - y^2$	110	-0.0296	-0.0200	-0.0345
$s_c s_c$	110	-0.0187	-0.0287	-0.0110
$XY XZ$	011	0.0169	0.00788	0.00845
$XY XY$	011	0.0159	0.00912	0.00883
$s_a x_a$	110	0.0148	-0.0184	0.0101
$x_a x_a$	110	0.0132	0.0148	0.0221
$x_a y_a$	110	0.0100	0.0154	0.0158
$x_a x_a$	011	-0.00851	-0.00727	-0.00902
$s_c XY$	110	0.00795	0.00137	-0.00961
$s_a s_a$	110	± 0.00565	± 0.00568	± 0.0159
$s_c z^2$	110	± 0.00466	± 0.0415	± 0.0512
$XY z^2$	110	± 0.00196	± 0.000836	± 0.00283
$z^2 z^2$	110	± 0.00127	± 0.00161	± 0.00687

Note: Subscripts a and c refer to anion and cation orbitals.

Section IV

2. Microwave Resonance in Ferromagnetic Chalcogenides

X-band magnetic resonance linewidth measurements on polycrystalline ferromagnetic chalcogenides have been continued.^{29,30}

Figure IV-13 shows the temperature dependence of the magnetic resonance linewidth from 77° to 199°K for CdCr₂Se₄. The qualitative behavior of the linewidth indicates a Curie temperature of approximately 130°K, in good agreement with the susceptibility measurements of Menyuk, et al.³¹ In the paramagnetic region, the g-factor was determined to be 1.99 ± 0.04.

Figure IV-14 indicates the results of similar measurements on CdCr₂S₄ from 72° to 169°K. Here, the Curie temperature is 86°K, while the g-factor in the paramagnetic region is 2.00 ± 0.04.

R. Weber
P. E. Tannenwald
J. W. Burke

3. Magnetic Resonance in Spiral Spinels

The normal cubic spinels ZnCr₂Se₄ and ZnCr₂S₄ have been investigated at millimeter wavelengths. ZnCr₂Se₄ is known to order in a co-planar antiferromagnetic spiral configuration below 21°K with the Cr³⁺ spin moments lying in the (001) plane and spiraling along the [001] axis. A discontinuity is observed in the microwave resonance field at the Néel temperature, suggesting the existence of a first-order transition. Resonances above and below T_N have been observed over the frequency range of 29.5 to 50.1 GHz. The paramagnetic resonances are consistent with a g = 2. The antiferromagnetic resonances at temperatures just below T_N obey the empirical equation $\omega = \gamma \sqrt{H_c^2 + H_o^2}$, where H_o is the applied field and H_c is an internal critical field characteristic of the material. At this temperature, the value of the internal field is 9.45 kOe as found from the zero-field resonance frequency of 26.4 GHz. Interpretation of the resonance data is complicated by the large susceptibility of this material, which leads to marked deviations from co-planarity at some of the magnetic fields used in this experiment.

Antiferromagnetic resonance has also been observed in ZnCr₂S₄ below the Néel temperature of 18°K. The data of zero-field resonance frequency vs temperature fit a Brillouin function with S = 3/2 and a zero temperature intercept at 67 GHz. The susceptibility of ZnCr₂S₄ is an order of magnitude lower than ZnCr₂Se₄, indicating a smaller deviation from co-planarity. No discontinuity in the resonance field was observed at T_N, and the antiferromagnetic resonance varied with temperature in a manner characteristic of a typical second-order antiferromagnetic phase transition.

J. J. Stickler

The following three subsections are abstracts of papers submitted to the Twelfth Annual Conference on Magnetism and Magnetic Materials to be held 15-18 November 1966 in Washington, D.C.

4. High Temperature Expansion of the Spin Correlation Function for the Classical Heisenberg Model

We report the results of extending the high temperature expansion of the zero-field static spin correlation function,³² and the corresponding extension of the susceptibility and specific heat series beyond the original "general spin"

Section IV

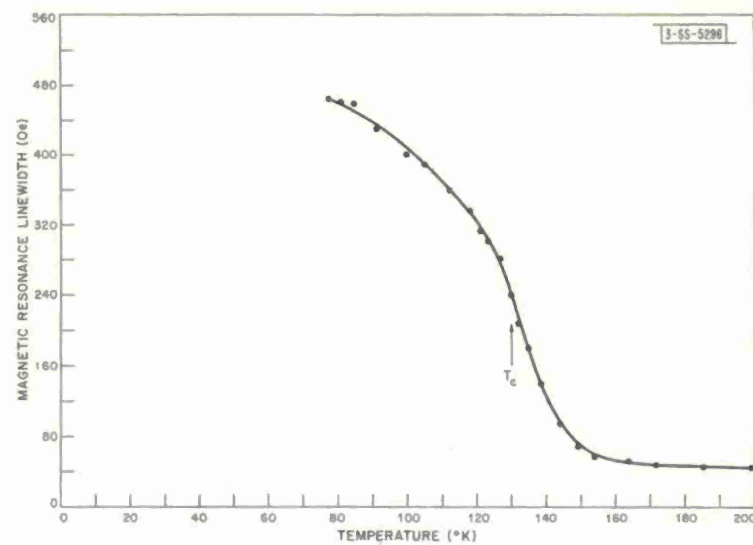


Fig. IV-13. Temperature dependence of magnetic resonance linewidth from 77° to 199°K for CdCr_2Se_4 .

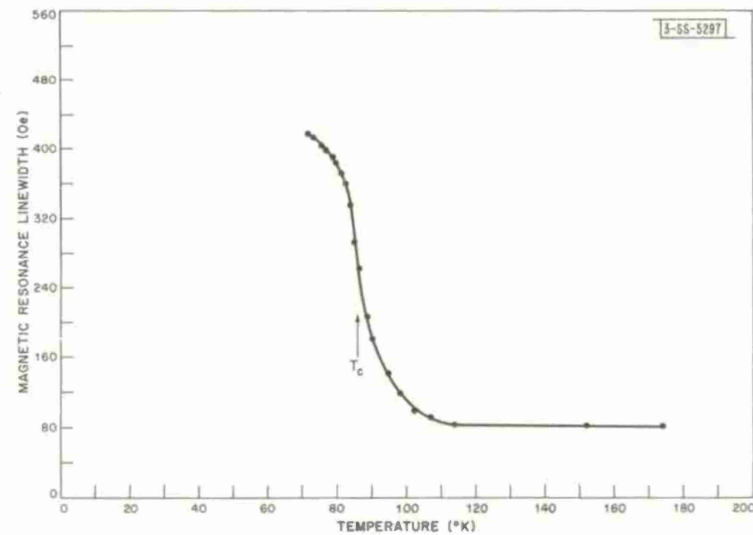


Fig. IV-14. Temperature dependence of magnetic resonance linewidth from 72° to 169°K for CdCr_2S_4 .

Section IV

calculation.³³ Our calculation is for the classical approximation to the Heisenberg model, in which the spin operators are replaced by isotropically interacting vectors of length $[S(S+1)]^{1/2}$. Although the results for this "classical Heisenberg model" are exact only in the infinite spin limit, we have found³² the classical approximation to be excellent for all values of the spin quantum number $S > 1/2$. Thus our extension of the high temperature series for $S \rightarrow \infty$ complements the recent extensions for $S = 1/2$.^{34,35}

H. E. Stanley

5. Dependence of the Critical Properties of Heisenberg Magnets on Spin and Lattice

High temperature expansion methods have recently been used to predict the form of the divergence of the zero-field static susceptibility χ at the critical temperature T_c . These studies have proposed the form $\chi \sim A(T - T_c)^{-\gamma}$, with $\gamma = 4/3$ independent of both lattice structure and spin quantum number S . In the present paper, we argue that this proposed behavior is inconsistent with the argument that led to the proposal, and that a consistent argument leads to a slow but nevertheless clear variation of γ with S . Our results are based on the six terms which are known for all S . They reduce to the special result, $\gamma = 1.43$ for $S = 1/2$, which was recently obtained,³⁴ and which was based on the larger number of terms available only for the special case of $S = 1/2$. We further point out that there exists at least one physically interesting lattice – a normal cubic spinel with nearest-neighbor ferromagnetic B-B interactions – for which the evidence indicates that γ may differ from $4/3$ by as much as 50 percent.

H. E. Stanley
T. A. Kaplan

6. Possibility of a Phase Transition for the Two-Dimensional Heisenberg Ferromagnet

We present evidence indicating the presence of a phase transition just as convincingly in the two-dimensional Heisenberg model with nearest-neighbor ferromagnetic interactions as in the three-dimensional case. The two-dimensional critical temperature, $T_c^{(2)}$, is found to be about half the ordering temperature T_M predicted by the Weiss molecular field approximation. Our evidence is provided by standard extrapolation procedures based upon the high temperature expansion in $1/T$ of the zero-field susceptibility per spin, χ . Further, we observe that the evidence favoring a simple power law divergence of χ at T_c , $\chi \sim (T - T_c)^{-\gamma}$, with $\gamma \approx 8/3$ in two dimensions is just as convincing as the evidence for $\gamma \approx 4/3$ in three dimensions. Finally, we point out that the "well-known result," $T_c^{(2)} = 0$, is not a valid conclusion from the Bloch spin wave argument.

H. E. Stanley
T. A. Kaplan

Section IV

C. TRANSPORT THEORY

1. Virial Theorem for the Homogeneous Electron Gas

The virial theorem for an interacting electron gas in a uniform background of positive charge was written down some time ago by March³⁶ in the form

$$2\bar{T} + \bar{V} = -r_s \frac{d\bar{E}}{dr_s} . \quad (9)$$

Here \bar{T} , \bar{V} , and \bar{E} are, respectively, the average kinetic, potential, and total energies per particle for the system in its ground state, and r_s is the radius of a sphere containing one electron in units of the Bohr radius. Although this relationship has been widely used, no proof has been given in the literature. It is usually stated that the proof of Cottrell and Paterson³⁷ for the virial theorem of interacting particles in a box suffices to justify Eq.(9) for the homogeneous electron gas. This is not so, because now we have the positive background and different boundary conditions.

We have established the relation (9) for the homogeneous electron gas in a positive background of charge. We have proved that

$$2\langle T \rangle + \langle V \rangle + r_s \frac{dE}{dr_s} = \int \Psi^*(H - E) \Phi d\tau \quad (10)$$

where $\langle T \rangle$ and $\langle V \rangle$ are the average kinetic and potential energies for the system in its ground state $\Psi(\vec{r}_1, \dots, \vec{r}_N)$ with energy E , H is the Hamiltonian of the system, and $\Phi = \sum_i \vec{r}_i \cdot \partial\Psi/\partial\vec{r}_i + r_s \partial\Psi/\partial r_s$. The right side of Eq.(10) vanishes under three different sets of boundary conditions (bc): (a) free bc, i.e., Ψ vanishes rapidly when $\vec{r}_i \rightarrow \infty$, (b) periodic bc over a cubic volume, and (c) infinite potential wall bc, i.e., Ψ vanishes where any \vec{r}_i is on the surface of the box. Under these three sets of bc, it can be proved that H is hermitian with respect to Ψ^* and Φ , and the integral in Eq.(10) vanishes, thereby establishing relation (9). Details of this work will appear in a separate report.

P.N. Argyres

2. Minimum Energy Slater Determinant for H^-

The following question has recently been posed:³⁸ Is a ground Slater determinant for the H^- ion bound? We report here a first step toward answering this question. We arbitrarily restrict ourselves to Slater determinants in which the electron spins are antiparallel and the space orbitals are spherically symmetrical. When one of the electrons is spatially unbound, the minimum total energy E is $-\frac{1}{2}$ a.u., the ground energy of the H atom. The essential question is then whether a determinant with E below $-\frac{1}{2}$ a.u. exists. We have shown, using a perturbation approach, that if one of the electrons is "nearly" spatially unbound, then $E \geq -\frac{1}{2}$ a.u., in the following precise sense.

Suppose that the space orbitals u_i of the Slater determinant $D = \det(u_1^\dagger u_2^\dagger)$ are spherically symmetrical and that

$$\lim_{\kappa \rightarrow 0} \int |\vec{r} - \vec{r}'|^{-1} |u_1(\kappa, r)|^2 d\vec{r} = 0 . \quad (11)$$

Then, for κ in the neighborhood of zero, $E(D) \geq -\frac{1}{2} \text{ a.u.}$, where $E(D)$ is the energy of D minimized with respect to u_2 . A Technical Note giving the proof of this result is in preparation.

P. D. Fleming
T. A. Kaplan
W. H. Kleiner

3. Energy Conversion in Nonhomogeneous Materials

Recent success in the growth of materials with sharp alloy concentration gradients has raised the question of whether the efficiency of energy converters can be improved by use of such alloys as compared to materials with uniform electrical properties.

In a theoretical analysis of this problem, the approach used in the literature for uniform materials³⁹ was combined with a method originally proposed by Steenbeck and Baranski⁴⁰, which was considerably generalized. The system under investigation is a material subjected to temperature, electric and magnetic fields along the x -, y -, and z -directions, with sharp gradient in the bandgap along the x -direction. The analysis was carried out with the assumption that isothermal conditions prevailed along y and z and that no current flows along x and z ; also, the laws of conservation of energy and charge, and the standard phenomenological transport equations³⁹ were utilized. The efficiency of the device was determined according to the relation $\eta = (\dot{\mathcal{E}}_o - \dot{\mathcal{E}}_L)/\dot{\mathcal{E}}_o$, where $\dot{\mathcal{E}}_o$ and $\dot{\mathcal{E}}_L$ are the rates of energy transfer past the hot and cold junctions, respectively. The theoretical efficiency, optimized by adjustment of the internal device resistance relative to the load resistance, is specified by the relations

$$\eta_T^* = \left[\frac{(1 + \delta_y^*) \mathfrak{A}_y}{\mathfrak{C}^2 \delta_y^* R_y L_y} - \frac{(1 + \delta_y^*) \mathfrak{B}_y}{\mathfrak{C} L_y} - g \delta_y^* \right]^{-1} \quad (12)$$

where

$$\mathfrak{A} \equiv -\langle \kappa \rangle \Delta_x T + \frac{1}{2} H_z^2 \left\langle \pi^2 \sigma^2 \frac{dT^2}{d\xi} \right\rangle$$

$$\mathfrak{B} \equiv H_z \left[\pi_o \sigma_o T_o + \left\langle \int_0^\xi T \frac{\partial(\pi \sigma)}{\partial \xi_1} d\xi_1 \right\rangle \right]$$

$$\mathfrak{C} \equiv H_z \frac{A_y}{L_y} \int_0^1 \pi \sigma \frac{dT}{d\xi} d\xi$$

$$\delta_y^* \equiv \left[1 - \frac{\mathfrak{B} \mathfrak{C} \bar{R}_y}{\mathfrak{A}} - \frac{g \mathfrak{C}^2 L_y \bar{R}_y}{A_y \mathfrak{A}} \right]^{1/2}$$

$$g \equiv \frac{\left\langle \int_0^\xi \sigma d\xi_1 \right\rangle}{\int_0^1 \sigma d\xi}$$

$$\bar{R}_y^{-1} \equiv \frac{A_y}{L_y} \int_0^1 \sigma d\xi$$

Section IV

and where κ , η , σ are the thermal conductivity, Nernst coefficient, and electrical conductivity; T is the temperature; A_y and L_y are the cross section perpendicular to and length along the y -axis, $\xi \equiv x/L_x$; and H_z is the applied magnetic field; $\Delta_x T = T_0 - T_L$; the subscripts zero and L refer to the hot and cold junctions located at $x = 0$ and L , respectively. For any function f , the symbol $\langle f \rangle$ represents the ratio

$$\left[\int_0^1 \frac{f}{\kappa} d\xi \right] \left[\int_0^1 \frac{1}{\kappa} d\xi \right]^{-1} . \quad (13)$$

It has been checked that the above relations reduce to the correct limiting expressions³⁹ that apply to materials with uniform properties. The specification of η requires (a) the solution of the differential equation for temperature⁴¹

$$\kappa \left(1 - \frac{H_z^2 \eta^2 T}{\kappa \rho} \right) \nabla_x^2 T + 2H_z \eta J^y \nabla_x T + \rho (J^y)^2 = 0 \quad (14)$$

where J^y is the current density along y , and (b) the specification of σ , η , and κ in their dependence on ξ . These matters will be made the subject of a later investigation.

J. M. Honig
B. Lax†

D. SCATTERING EXPERIMENTS WITH LASERS

1. Stimulated Brillouin Scattering in Quartz at 2.1° to 300°K

We have made a study of stimulated Brillouin scattering in single-crystal quartz over the temperature range 2.1° to 300°K. At various temperatures, we have calculated the velocity of sound from the Brillouin shifts. Contrary to a recent report by Russian workers,⁴² we find no increase in the Stokes shift at temperatures below 80°K. Even at 2.1°K, where Krivokhizha, et al., observe an anomalous increase in the Stokes component of 2.5 times for a z-directed high-intensity ruby laser beam, we measure the usual Brillouin shift corresponding to the normal velocity of sound. The Russian workers suggested several possible approaches to explain their results, such as the effect of an intense electric field on the index of refraction or on the velocity of sound. Although such extreme nonlinear phenomena would be exceedingly interesting, our quartz scattering experiments do not appear to be the basis for their existence.

Our experiments were carried out with a high-power ruby laser attenuated to approximately 3 MW in order to avoid or minimize damage to the sample and optical components in the beam path. At 2.1°K at this power level, we usually observe one or two Brillouin shifts with the exciting radiation traveling along the x - or z -direction. In either case, the shifts are the same, respectively, as those measured at room temperature within the experimental accuracy of about 5 percent. We do, however, observe on occasion a weak additional line which, because of its

† National Magnet Laboratory, M.I.T.

relative displacement with respect to successive interference orders of the etalon, is not associated with the Brillouin shifts. The occurrence of this line is compatible with the 466 cm^{-1} Raman line of quartz.

P. E. Tannenwald C. D. Parker
J. B. Thaxter F. H. Perry

2. Second Harmonic Rayleigh Scattering in Liquids

The measured temperature dependence of second harmonic Rayleigh scattering in CCl_4 and water is given in Figs. IV-15 and IV-16.

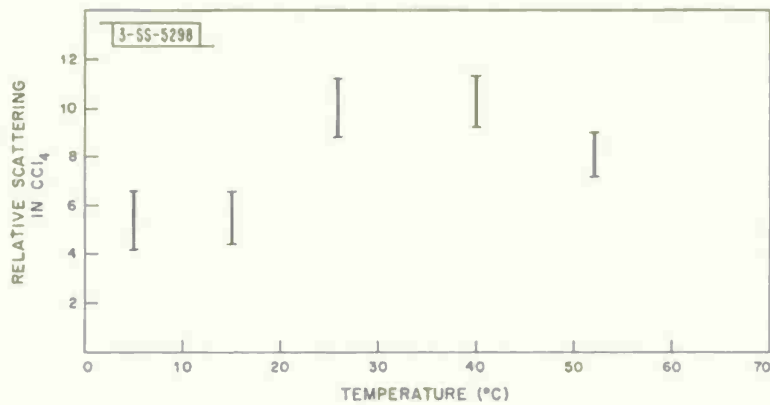


Fig. IV-15. Second harmonic Rayleigh scattering in CCl_4 as a function of temperature.

The scattering process responds to high-frequency motions, up to about the optical frequency itself, but the molecular orientation relaxation frequency is only about 10^{11} Hz . Therefore, the experiment measures effectively instantaneous orientational configurations, as is usual in scattering experiments.

A calculation has been made, including internal optical and internal static fields, but neglecting orientation correlation. Although complete data on the polarizabilities are not available, it appears that the third rank polarizability tensor contribution to the (static) field-dependent polarizability is dominant in molecules of low symmetry, as has been assumed previously; but, surprisingly, the fourth rank polarizability is dominant for tetrahedral molecules. This explains qualitatively the rapid decrease of scattering observed by Maker and Terhune in CCl_4 on approach to boiling.

Let the dipole moment m_α of an isolated molecule in an electric field G_α be

$$m_\alpha = \mu_\alpha + \alpha_{\alpha\beta} G_\beta + \frac{1}{2} \beta_{\alpha\beta\gamma} G_\beta G_\gamma + \frac{1}{6} \gamma_{\alpha\beta\gamma\delta} G_\beta G_\gamma G_\sigma + \dots \quad (15)$$

The tensors are approximately symmetric in frequency ranges in which the liquids are transparent. The local fields F_α are accounted for by replacing $\beta_{\alpha\beta\gamma}$ in the scattering formulas for $F_\alpha = 0$ by

$$\begin{aligned} \sigma_{\alpha\beta\gamma}^{(i)} &\equiv [\partial^2 m_\alpha^{(i)} / \partial E_\gamma^{(i)} \partial E_\beta^{(i)}]_{E=0} \\ &= \beta_{\alpha\beta\delta}^{(i)} [\delta_{\gamma\delta} + 2\partial F_\delta^{(i)} / \partial E_\gamma^{(i)} + \dots] + \gamma_{\alpha\beta\gamma\delta}^{(i)} F_\delta^{(i)} + \dots \end{aligned} \quad (16)$$

Section IV

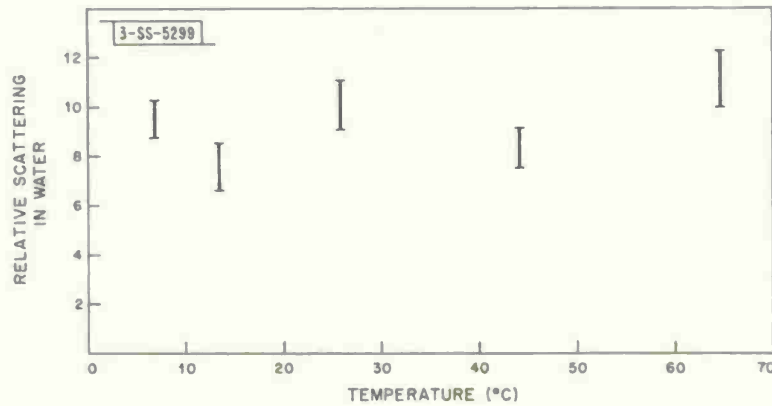


Fig. IV-16. Second harmonic Rayleigh scattering in water as a function of temperature.

where $E_{\alpha}^{(i)}$ is the value at the i^{th} molecule of a plane-wave optical field in the medium, and $G_{\alpha} = E_{\alpha} + F_{\alpha}$.

The effect of the induced local optical field, represented by $\partial F_{\delta}/\partial E_{\gamma}$, is customarily included by multiplying the applied field by the Lorentz factor $L_{\omega} \equiv \frac{1}{2}(n_{\omega}^2 + 2)$. (However, an additional factor ⁴³ $L_{2\omega}$, used in second harmonic generation, is not appropriate, because the polarization at 2ω is incoherent.) The deviations from this description have been calculated for the present problem and are negligible. Taking

$$J \equiv \sum_{i,j} \langle \sigma_{\alpha\beta\gamma}^{(i)} \sigma_{\alpha\beta\gamma}^{(j)} \rangle$$

and

$$K \equiv \sum_{i,j} \langle \sigma_{\alpha\alpha\beta}^{(i)} \sigma_{\beta\gamma\gamma}^{(j)} \rangle \quad (17)$$

we find for the (time-averaged) z -polarized scattering along the y -direction, of a z -polarized beam incident along x ,

$$I_z \propto (6J + 9K) \quad (18)$$

and for the z -polarized scattering

$$I_x \propto (4J - K) \quad (19)$$

with macroscopic proportionality factors. The resulting depolarization I_x/I_z is equivalent, for a perfect gas, to a formula given previously.⁴⁴

The relative importance of the terms in $\sigma_{\alpha\beta\gamma}$ will be considered for tetrahedral molecules, and then for polar molecules. A useful coordinate system for tetrahedral molecules is the one formed by three perpendicular edges of the cube, four of whose corners are the vertices of the i^{th} molecule. In this coordinate system, $\beta_{\alpha\beta\gamma}|_{\beta=\alpha} = 0$ and $\beta_{123}^{(i)} \equiv \beta$. Using this, we have

$$J = \sum_{i,j} \langle \beta_{\alpha\beta\gamma}^{(i)} \beta_{\alpha\beta\gamma}^{(j)} + \gamma_{\alpha\beta\gamma\delta}^{(i)} F_{\delta}^{(i)} \gamma_{\alpha\beta\gamma\sigma}^{(j)} F_{\sigma}^{(j)} \rangle$$

and

$$K = \langle \gamma_{\alpha\alpha\beta\delta}^{(i)} F_{\delta}^{(i)} \gamma_{\beta\gamma\gamma\sigma}^{(j)} F_{\sigma}^{(j)} \rangle . \quad (20)$$

In the cubic coordinate system, the only independent components of $\gamma_{\alpha\beta\gamma\delta}$ are⁴⁵ $\gamma_{1111} = \gamma_{2222} = \gamma_{3333} = \gamma_1$, and $\gamma_{1122} = \gamma_{2233} = \gamma_{3311} = \gamma_2$. If we ignore intermolecular orientation correlation,

$$\begin{aligned} N^{-1}J &= 6\beta^2 + (\gamma_1^2 + 6\gamma_2^2) \langle F_{\alpha} F_{\alpha} \rangle \\ N^{-1}K &= (\gamma_1 + 2\gamma_2)^2 \langle F_{\alpha} F_{\alpha} \rangle \end{aligned} \quad (21)$$

for N molecules. Unlike the present case, Rayleigh scattering can be evaluated relatively accurately, because the second rank polarizability tensors of all molecules are approximately the same, independently of orientation.

The data for comparison of the terms are most readily available for CH_4 . Here $|\beta| = 10^{-32}$ esu, from second harmonic Rayleigh scattering in the gas;⁴⁶ $3\gamma_2 \approx \gamma_1 = 2.6 \times 10^{-36}$ esu, calculated⁴⁷ from the measured Kerr constant; and $\langle F^2 \rangle = 1 \times 10^{11}$ esu, calculated⁴⁸ by setting $1/2 N\alpha \langle F^2 \rangle$ equal to the latent heat of vaporization. Then $(5/3) \gamma_1^2 \langle F^2 \rangle / 6\beta^2 \approx 2000$. That the higher order term gives a much larger contribution results from the near approach of a tetrahedral molecule to a sphere, for which $|\beta| = 0$, but $|\gamma_1|$ remains finite. The term $|\beta|$ of CH_4 is three orders of magnitude smaller than a typical element $|\beta_{\alpha\beta\gamma}|$ of CHCl_3 , estimated⁴⁸ from the depolarization of Rayleigh scattering. Of this, only one order of magnitude is immediately attributable to the atomic number ratio, 7.4. The fifth rank polarizability must similarly be small for tetrahedral molecules, so that the scattering is dominated by the $\gamma F \gamma F$ term.

The $\gamma F \gamma F$ term does not occur in a gas, so that the scattering per molecule should be much greater in the liquid. The scattering in liquid CCl_4 has been observed⁴⁹ to decrease on approach to the boiling point, 77°C, and almost completely disappears at the boiling point, in agreement with this theory.

For general molecules, again neglecting orientation correlation,

$$N^{-1}J = \langle (\beta_{\alpha\beta\gamma} + \gamma_{\alpha\beta\gamma\delta} F_{\delta}) (\beta_{\alpha\beta\gamma} + \gamma_{\alpha\beta\gamma\sigma} F_{\sigma}) \rangle . \quad (22)$$

The independent components of the polarizability tensors for water, a polar molecule, with the z-axis along the molecular dipole, are⁴⁵ $\beta_{111}, \beta_{223}, \beta_{333}, \gamma_{1111}, \gamma_{2222}, \gamma_{3333}, \gamma_{1122}, \gamma_{2233}$, and γ_{3311} . From the Onsager theory, the local static field F_3 is

$$F_3 = \frac{2}{3} \frac{(n_O^2 - 1)(n_{\omega}^2 - 1)}{(2n_O^2 + n_{\omega}^2)} \frac{\mu_3}{\alpha} . \quad (23)$$

Taking, crudely, all the nonzero components of $\beta_{\alpha\beta\gamma}$ to be the same, β , and all the nonzero components of $\gamma_{\alpha\beta\gamma\delta}$ to be the same, γ , we have

$$(7N)^{-1}J = (9N)^{-1}K = \beta^2 + 2\beta\gamma F_3 + \gamma^2 \langle F_{\alpha} F_{\alpha} \rangle . \quad (24)$$

Section IV

When we use $\beta = 10^{-29}$ esu and $F_3 = 10^4$ esu (the values⁴⁸ for CHCl_3), and $\langle F^2 \rangle = 1 \times 10^{11}$ esu, the terms in F are negligible compared to β^2 . This suggests that local fields are negligible for polar molecules.

There are still other molecules, such as *cis*- C_2Cl_6 , which are non-centrosymmetric, but are neither tetrahedral nor polar.

D. L. Weinberg

3. Raman Scattering from Plasmons Interacting with LO Phonons in GaAs

Raman scattering from charge carrier plasmons has been observed for the first time in a solid. As the carrier concentration of the samples is increased from $n = 2.3 \times 10^{15} \text{ cm}^{-3}$ to $n = 2.9 \times 10^{18} \text{ cm}^{-3}$, the plasma frequency sweeps through the longitudinal optical phonon frequency. When the plasma frequency approaches the phonon frequency, the LO phonon line observed in Raman scattered light broadens and shifts to higher frequency as shown in Fig. IV-17. A second, small broad line at lower frequency appears and approaches the transverse optical phonon frequency as the carrier concentration increases. In the limit of high electron concentration, the LO phonon mode vibrates at the TO frequency, because the charge carriers have shielded out the polarization of the lattice vibrations. The transverse optical phonon line is unaffected by carrier concentration. These results constitute a particularly clear experimental verification of the recently predicted⁵⁰⁻⁵² theoretical behavior of the plasmon-phonon system.

The Raman scattered light was generated in room-temperature samples by a 1.0648-micron YAG laser, operated CW at 1 watt. It was observed at 90° with a Spex Model 1400 double monochromator and an S-1 photomultiplier. The gratings used were blazed at 0.75 micron. The fall-off of sensitivity toward longer wavelengths as a consequence of the combined spectral response of the S-1 photomultiplier and the 0.75-micron blazed gratings caused the anti-Stokes radiation to appear greater in intensity than the Stokes radiation. Ability to observe both Stokes and anti-Stokes radiation was a great help in discriminating against luminescence which sometimes occurred. The data in Fig. IV-17 are recorder traces which have been hand smoothed in some cases. Signal-to-noise ratios of the TO lines were in excess of 100 for the purest samples,

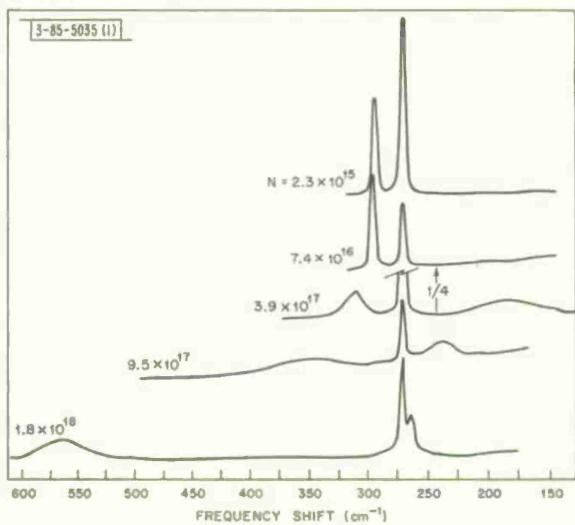


Fig. IV-17. Anti-Stokes Raman spectrum of n-type GaAs. Frequency shift scale is not linear.

and in excess of 20 in all cases. At the higher carrier concentrations, the solubility limit of donors in GaAs is being approached, and there was some difficulty with sample inhomogeneity. The two points on the upper branch of the curve in Fig. IV-18 for the sample with $n = 1.7 \times 10^{18} \text{ cm}^{-3}$ occurred for two runs where different portions of the sample were illuminated by the laser beam.

Varga⁵¹ has shown that in the long wavelength limit, the valence electrons, the polar lattice vibrations, and the conduction electrons make additive contributions to the total dielectric response function:

$$\epsilon_T(0, \omega) = \epsilon_{\infty} + \frac{\epsilon_0 - \epsilon_{\infty}}{1 - \omega_p^2/\omega_t^2} - \frac{\omega_p^2 \epsilon_{\infty}}{\omega^2} \quad (25)$$

where

$$\omega_p^2 = \frac{4\pi n e^2}{m^* \epsilon_{\infty}}$$

For longitudinal waves, the eigenfrequencies of the system are given by the zeros of the dielectric response:

$$x^2 = \frac{1}{2} [\alpha + y^2 \pm \sqrt{(\alpha + y^2)^2 - 4y^2}] \quad (26)$$

where we have written $x = \omega/\omega_t$, $y = \omega_p/\omega_t$, and $\alpha = \epsilon_0/\epsilon_{\infty} = \omega_l^2/\omega_t^2$. Since all the constants in Eq. (25) are accessible to independent measurement, the solid lines showing the eigenfrequencies in Fig. IV-18 contain no adjustable parameters. In the sample containing $n = 2.5 \times 10^{15} \text{ cm}^{-3}$ carriers, where the interaction with carriers is negligible, we obtain $\omega_t = 268 \text{ cm}^{-1}$ and $\omega_l = 291 \text{ cm}^{-1}$ from the data of Fig. IV-17, and hence $\alpha = 1.179$. We take $m^* = 0.07$ and $\epsilon_{\infty} = 11.3$ (Ref. 53) for the calculation of ω_p . The relative phonon content of the two coupled modes in

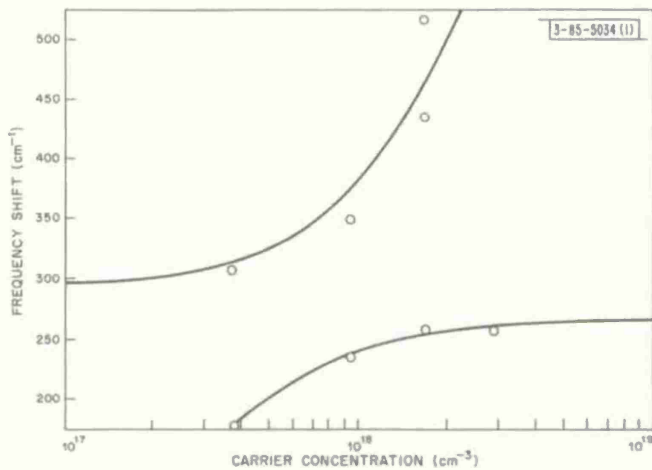


Fig. IV-18. Plasmon-LO phonon interaction in GaAs. Solid lines are calculated from Eq. (26) for $\omega_t = 268 \text{ cm}^{-1}$, $\omega_l = 291 \text{ cm}^{-1}$, $\epsilon_{\infty} = 11.3$, $m^* = 0.07$.

Section IV

Fig. IV-18 is of interest. Varga has defined a phonon strength $S_m = |\langle m | \varphi | 0 \rangle|^2$, where $\langle m |$ is the one-phonon function in the m^{th} level, and φ is the phonon operator. He finds the interesting sum rule $\sum_m \omega_m S_m = \omega_\ell$. The phonon strength is given by

$$S_m = \frac{\alpha^{1/2}(\alpha - 1) x_m^3}{(\alpha - 1) x_m^4 + y^2(1 - x_m^2)^2} \quad . \quad (27)$$

We see from the curves of phonon strength in Fig. IV-19, that the Raman lines on the low-frequency side of the TO mode range in phonon strength from $S = 0.3$ for the $n = 3.8 \times 10^{17} \text{ cm}^{-3}$ sample to $S = 1.05$ for $n = 3 \times 10^{18} \text{ cm}^{-3}$. The Raman lines on the high-frequency side of the TO mode have $S \approx 1.0$ for $n = 2.5 \times 10^{15} \text{ cm}^{-3}$ down to $S = 0.05$ for the line with the greatest frequency shift. This line may then be regarded as due to almost pure plasmon scattering.

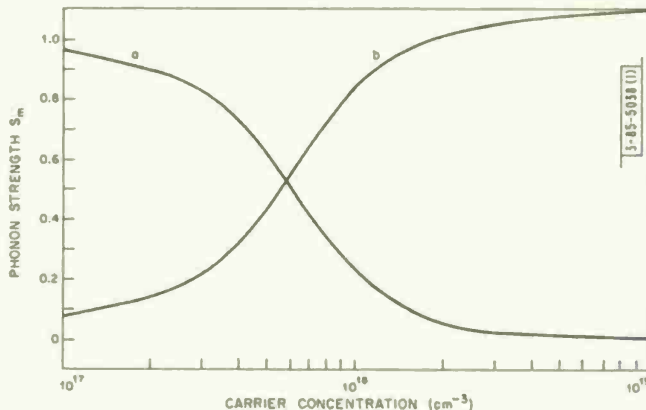


Fig. IV-19. Phonon strengths of interacting plasmon-LO phonon modes in GaAs. Curve a is for high-frequency mode; curve b is for low-frequency mode.

The Raman cross section for scattering by phonons has been treated in third-order perturbation by Loudon,⁵⁴ and intraband contributions to the plasmon cross section have been calculated by McWhorter⁵⁵ and Platzman.⁵⁶ The importance of interband contributions to the plasmon cross section has been pointed out by Wolff.⁵⁷ While no theoretical treatment has been given for the cross section of the interacting plasmon-phonon system, the cross section for a given line should be proportional to the phonon or plasmon content of the mode at that frequency. Our ability to determine intensity and linewidth in the mixed mode lines has been limited by the homogeneity of the samples presently available to us. The importance of inhomogeneity for line-breadth measurements will be proportional to the slope of the curves in Fig. IV-18, and the slope is greatest for modes with the greatest plasmon content. We see in Fig. IV-17 that the Raman lines with low plasmon content are indeed narrower, as expected. Although absolute intensity measurements are difficult, an intrinsic property of the crystal, the TO mode intensity, serves as a good relative reference level.

A. Mooradian
G. B. Wright

4. First-Order Raman Effect in III-V Compounds

The first-order Raman effect for GaAs, InP, AlSb, and GaP has been measured at 1.06 microns. These results represent the first observation of infrared Raman spectra for solids and of Raman scattering in GaAs, InP, and AlSb. The measurements were made at room temperature and liquid helium temperature, and also at 200°C for GaP. The results are presented in Table IV-2, along with values deduced by other methods. A more detailed discussion is to be published in the September 1966 issue of Solid State Communications.

A. Mooradian
G. B. Wright

TABLE IV-2
TRANSVERSE AND LONGITUDINAL FREQUENCIES FOR LONG WAVELENGTH PHONONS

Compound	Reference	Method	Temperature	$\bar{\nu}_t$ (cm ⁻¹)	$\bar{\nu}_l$ (cm ⁻¹)
GaAs	Present measurements	Raman	Room	268.6 ± 0.3	291.9 ± 0.3
		Raman	Helium	273.1 ± 0.3	296.4 ± 0.3
	60	Transmission	Helium	272.4 ± 0.5	294.2 ± 0.5
	63	Reflection	Helium	273.3 ± 3	297.3 ± 2
	60	Transmission	Room	268.2 ± 0.5	290.5 ± 0.5
	60	Reflection	Room	268.2 ± 0.5	291.5 ± 0.5
	61	Neutron	Room	267 ± 3	285 ± 6
InP	62	Tunneling	Helium		282 ± 4
	Present measurements	Raman	Room	303.7 ± 0.3	345.0 ± 0.3
		Raman	Helium	308.2 ± 0.3	349.5 ± 0.3
	63	Reflection	Room	307 ± 8	351 ± 5
	62	Tunneling	Helium		363 ± 12
AlSb	64	Emissivity	Room	311	339
	Present measurements	Raman	Room	318.9 ± 0.5	339.9 ± 0.5
		Raman	Helium	323.4 ± 0.5	344.4 ± 0.5
	63	Reflection	Room	318.8 ± 0.5	339.6 ± 0.5
	63	Reflection	Room	318 ± 8	345 ± 5
GaP	Present measurements	Romont†	Room	367.3 ± 1	403.0 ± 0.5
		Raman†	Helium	365.6 ± 1	403.0 ± 0.5
	65	Raman	200°C	359.3 ± 1	397.0 ± 0.5
		Reflection	Room	366.3 ± 0.6	

† These results are in essential agreement with those of Refs. 58 and 59.

Section IV

5. Landau Level Raman Scattering

The cross section has been calculated for scattering of light by electrons, the electrons making transitions between Landau levels in the conduction band of a semiconductor. The Landau level selection rule is $\Delta n = \pm 2$ or 0. Including spin flip, we find three Stokes processes if the spin-up state, $n = 0$, is the initial electronic state. The three final states are $n = 2$, $m_s = \pm \frac{1}{2}$ and $n = 0$, $m_s = -\frac{1}{2}$. By using states in the degenerate valence band as virtual intermediate states, as for InSb, and assuming the photon frequency is a reasonable fraction of the bandgap energy, the cross section for $n = 0$, $m_s = -\frac{1}{2}$ final state is found to be independent of cyclotron frequency to lowest order. This should be compared with the calculation of Wolff⁵⁷ for two nonparabolic bands, where a cross section for $n = 2$ final states was found which is proportional to the square of the cyclotron frequency. The present cross section is approximately a factor of $(\omega_g / \omega_c)^2$ greater than that of Wolff. In the case of InSb in a 30-kG field, this gives a cross section about two orders of magnitude larger for the spin flip, but no change in Landau level process. Further work is being carried out concerning selection rules and the possibility of observing by Raman scattering other magnetic field dependent effects.

P. L. Kelley
G. B. Wright

REFERENCES

1. B. O. Seraphin and R. B. Hess, Phys. Rev. Letters 14, 138 (1964).
2. K. L. Shaklee, F. H. Pollak and M. Cardona, Phys. Rev. Letters 15, 883 (1965).
3. A. Frova and P. J. Boddy, Phys. Rev. Letters 16, 688 (1966).
4. Solid State Research Report, Lincoln Laboratory, M.I.T. (1966:1), DDC 632998, H-721.
5. B. Batz, Solid State Commun. 4, 241 (1966).
6. A. K. Ghosh, Phys. Rev. Letters (to be published).
7. J. Feinleib, Phys. Rev. Letters 16, 1200 (1966).
8. J. G. Mavroides, M. Dresselhaus, R. L. Aggarwal and G. Dresselhaus, Tokyo International Conference on Physics of Semiconductors, 1966 (to be published).
9. G. Dresselhaus, A. F. Kip and C. Kittel, Phys. Rev. 98, 368 (1955).
10. Solid State Research Report, Lincoln Laboratory, M.I.T. (1966:2), p. 39.
11. B. Lax and S. Zwerdling, Progress in Semiconductors (Heywood and Company Ltd., London, 1960), Vol. 5, p. 223.
12. S. H. Groves, C. Pidgeon and J. Feinleib (to be published); also Sec. IV-A-4 of this report.
13. S. Zwerdling, W. H. Kleiner and J. P. Theriault, J. Appl. Phys. Suppl. 32, 2118 (1961).
14. Solid State Research Report, Lincoln Laboratory, M.I.T. (1965:2), p. 57. DDC 624611, H-686.
15. P. Fisher and H. Y. Fan, Phys. Rev. Letters 2, 456 (1959).
16. H. N. Spector, Phys. Rev. 125, 1880 (1962).
17. M. H. Cohen, M. J. Harrison and W. A. Harrison, Phys. Rev. 117, 937 (1960).
18. N. Takimoto, Progr. Theoret. Phys. 25, 327 (1961).
19. K. W. Nill and A. L. McWhorter, 1965 Ultrasonics Symposium, Boston, 1-4 December 1965.
20. Y. Katayama and S. Tanaka, Phys. Rev. Letters 16, 129 (1966).
21. R. P. Khosla and R. J. Sladek, Phys. Rev. Letters 15, 521 (1965).
22. E. J. Johnson and D. M. Larsen, Phys. Rev. Letters 16, 655 (1966).
23. R. J. Elliot and R. Loudon, J. Phys. Chem. Solids 15, 196 (1960).
24. J. C. Slater and G. F. Koster, Phys. Rev. 94, 1498 (1954).
25. Ref. 4, p. 43.
26. W. D. Davidon, ANL 5990 Rev., Argonne National Laboratory (1959).
27. C. S. Naiman, et al., J. Appl. Phys. 36, 1044 (1965).
28. W. C. Koehler and E. O. Wollan, J. Phys. Chem. Solids 2, 100 (1957).
29. Ref. 4.
30. Ref. 10, p. 46.
31. Ref. 14, p. 63.
32. H. E. Stanley and T. A. Kaplan, Phys. Rev. Letters 16, 981 (1966).
33. G. S. Rushbrooke and P. J. Wood, Mol. Phys. 1, 257 (1958).
34. G. A. Baker, H. E. Gilbert, J. Eve and G. S. Rushbrooke, Phys. Letters 20, 146 (1966).
35. C. Domb and D. W. Wood, Proc. Phys. Soc. 86, 1 (1965).
36. N. H. March, Phys. Rev. 110, 604 (1958).
37. T. L. Cottrell and S. Paterson, Phil. Mag. 42, 391 (1951).

Section IV

38. T. A. Kaplan and W. H. Kleiner (to be published).
39. T. C. Harman and J. M. Honig, *J. Appl. Phys.* 33, 3178, 3188 (1962).
40. M. Steenbeck and P. I. Baranskii, *Soviet Phys. - Tech. Phys.*, JETP 1, 1345 (1957).
41. C. F. Kooi, R. B. Hurst, K. F. Cuff and S. R. Hawkins, *J. Appl. Phys.* 34, 1735 (1963).
42. S. V. Krivokhizha, et al., *JETP Letters* 3, 245 (1 May 1966).
43. R. W. Terhune, P. D. Maker and C. M. Savage, *Phys. Rev. Letters* 14, 681 (1965).
44. S. J. Cyvin, J. E. Rauch and J. C. Decius, *J. Chem. Phys.* 43, 4085 (1965).
45. R. Fieschi, *Physica* 24, 972 (1957).
46. P. D. Maker, Physics of Quantum Electronics, edited by P. L. Kelley, B. Lax and P. E. Tannenwald (McGraw-Hill, New York, 1966).
47. A. D. Buckingham and J. A. Pople, *Proc. Phys. Soc. (London)* A68, 905 (1955).
48. A. D. Buckingham and M. J. Stephen, *Trans. Faraday Soc.* 53, 884 (1957).
49. P. D. Maker, private communication; R. W. Terhune, Seminar, M.I.T., May 1966.
50. I. Yokota, *J. Phys. Soc. Japan* 16, 2075 (1961).
51. B. B. Varga, *Phys. Rev.* 137, A1896 (1965). This contains references to earlier work in nondegenerate systems.
52. Y. C. Lee and N. Tzoar, *Phys. Rev.* 140, A396 (1965); K. S. Singwi and M. P. Tosi, *Phys. Rev.* (to be published).
53. D. T. F. Marple, *J. Appl. Phys.* 35, 1241 (1964).
54. R. Loudon, *Proc. Roy. Soc. (London)* A275, 218 (1963).
55. A. L. McWhorter, Physics of Quantum Electronics, Conference Proceedings, edited by P. L. Kelley, B. Lax and P. E. Tannenwald (McGraw-Hill, New York, 1966), p. 111.
56. P. M. Platzman, *Phys. Rev.* 139, A379 (1965).
57. P. A. Wolff, *Phys. Rev. Letters* 16, 225 (1966).
58. M. V. Hobden and J. P. Russell, *Phys. Letters* 13, 39 (1964).
59. J. P. Russell, *J. DePhysique* 26, 620 (1965).
60. S. Iwasa, I. Balslev and E. Burstein, Proceedings of the 7th International Conference on the Physics of Semiconductors, Paris, 1964 (Dunod, Paris, 1964), p. 1077.
61. J. L. T. Waugh and D. Dolling, *Phys. Rev.* 132, 2410 (1963).
62. R. N. Hall and J. H. Racette, *J. Appl. Phys.* 32, 2078S (1961).
63. M. Hass and B. W. Henvis, *J. Phys. Chem. Solids* 23, 1099 (1962).
64. D. L. Stierwalt and R. F. Potter, Proceedings of the 7th International Conference on the Physics of Semiconductors, Paris, 1964 (Dunod, Paris, 1964), p. 1073.
65. D. A. Kleinman and W. G. Spitzer, *Phys. Rev.* 118, 110 (1960).

UNCLASSIFIED

DOCUMENT CONTROL DATA - R&D

(Security classification of title, body of abstract and indexing annotation must be entered when the overall report is classified)

BY
JOHN TRUMBULL,
LAWYER AND HISTORIAN,
OF NEW YORK.

IN TWO VOLUMES.

PRICE,

50

DOLLARS.

1805.

1806.

1807.

1808.

1809.

1810.

1811.

1812.

1813.

1814.

1815.

1816.

1817.

1818.

1819.

1820.

1821.

1822.

1823.

1824.

1825.

1826.

1827.

1828.

1829.

1830.

1831.

1832.

1833.

1834.

1835.

1836.

1837.

1838.

1839.

1840.

1841.

1842.

1843.

1844.

1845.

1846.

1847.

1848.

1849.

1850.

1851.

1852.

1853.

1854.

1855.

1856.

1857.

1858.

1859.

1860.

1861.

1862.

1863.

1864.

1865.

1866.

1867.

1868.

1869.

1870.

1871.

1872.

1873.

1874.

1875.

1876.

1877.

1878.

1879.

1880.

1881.

1882.

1883.

1884.

1885.

1886.

1887.

1888.

1889.

1890.

1891.

1892.

1893.

1894.

1895.

1896.

1897.

1898.

1899.

1900.

1901.

1902.

1903.

1904.

1905.

1906.

1907.

1908.

1909.

1910.

1911.

1912.

1913.

1914.

1915.

1916.

1917.

1918.

1919.

1920.

1921.

1922.

1923.

1924.

1925.

1926.

1927.

1928.

1929.

1930.

1931.

1932.

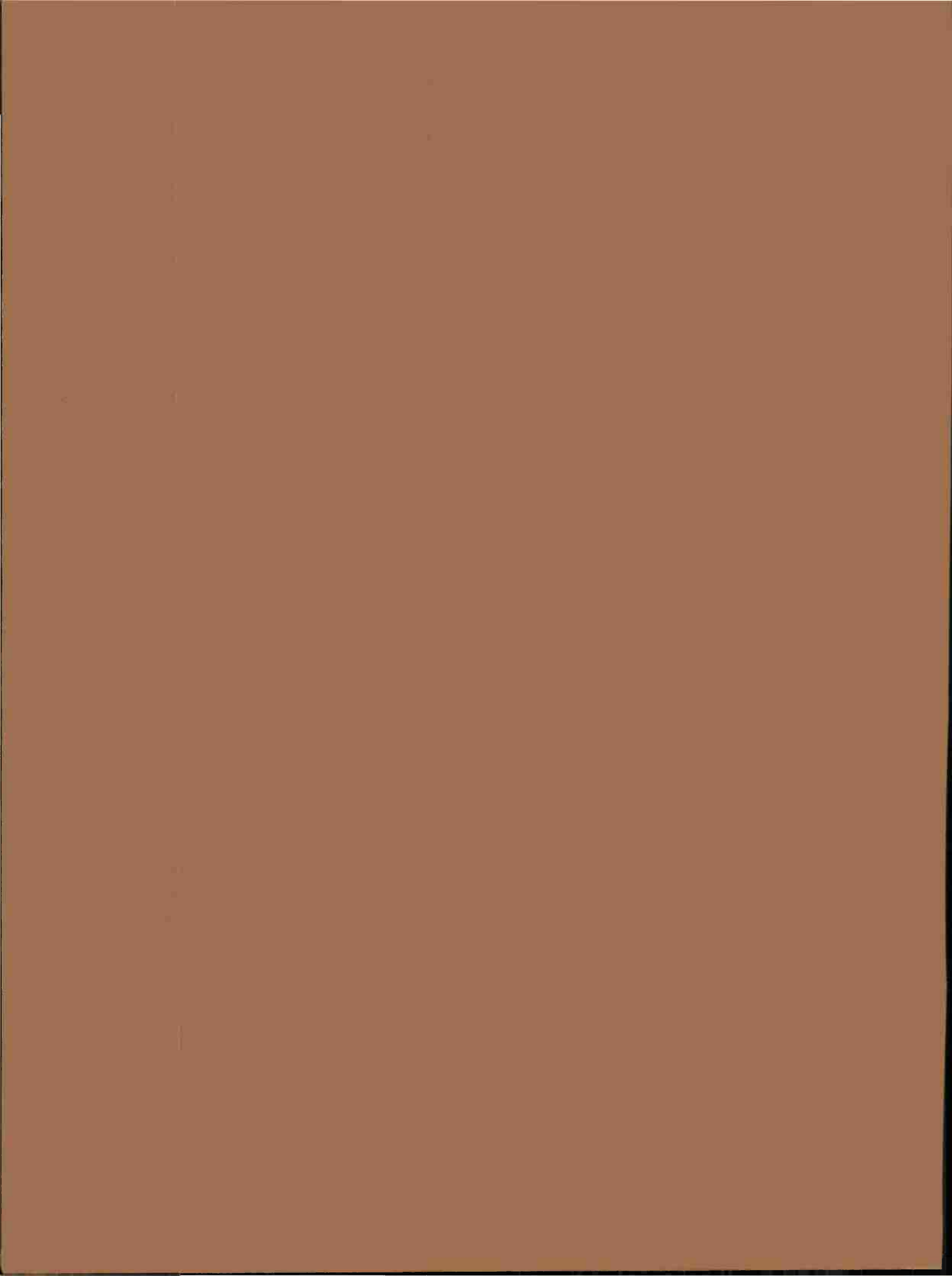
1933.

1934.

1935.

1936.

1937.



Printed by
United States Air Force
L. G. Hanscom Field
Bedford, Massachusetts